Supporting Information for

Electrochemical CO_2 Reduction Catalyzed by Atomically Precise Alkynyl-Protected Au_7Ag_8, Ag_9Cu_6, and $Au_2Ag_8Cu_5$ Nanoclusters: Probing the Effect of Multi-metal Core on Selectivity

Xiaoshuang Ma,‖[a] Fang Sun,‖[b] Lubing Qin,[a] Yonggang Liu,[a] Xiongwu Kang,[a] Likai Wang,[c] De-en Jiang,[d] Qing Tang,*[b] & Zhenghua Tang*[a,e]

[a] New Energy Research Institute, Guangdong Provincial Key Laboratory of Atmospheric Environment and Pollution Control, School of Environment and Energy, South China University of Technology, Guangzhou Higher Education Mega Centre, Guangdong, 510006, China

E-mail: zhht@scut.edu.cn

[b] School of Chemistry and Chemical Engineering, Chongqing Key Laboratory of Theoretical and Computational Chemistry, Chongqing University, Chongqing, 401331, China

E-mail: qingtang@cqu.edu.cn

[c] School of Chemistry and Chemical Engineering, Shandong University of Technology, Shandong, 255049, China

[d] Department of Chemistry, University of California, Riverside, CA, 92521, United States

[e] Guangdong Provincial Key Laboratory of Functional Supramolecular Coordination Materials and Applications, Jinan University, Guangdong, 510632, China

‖ X. Ma and F. Sun: The two authors contributed equally to this work

Table of Contents

Figure S26. The overall mechanism of CO formation via the proton mechanism and formate formation via the hydride-proton mechanism from CO_2 reduction on $[Au_2Ag_8Cu_5(C{\equiv}C\text{-}CH_3)_{11}]^+$.

Figure S27. Schematic presentation of adsorption structures of *COOH, *CO and *H intermediates on $[Au_7Ag_8(C{\equiv}C\text{-}^tBu)_{12}]^+$ and $[Au_7Ag_8(C{\equiv}C\text{-}^tBu)_{11}]^+$, respectively. Comparison of CO_2RR vs. HER on Au_7Ag_8 with $\text{-}C{\equiv}C\text{-}^tBu$ and $\text{-}C{\equiv}C\text{-}CH_3$ ligand protection.

Supporting Tables

Table S1. The XPS data of $Au_2Ag_8Cu_5$.

Table S2. Molar absorption coefficients (ε) of $Au_2Ag_8Cu_5$.

Table S3. Summary of the calculated yields of $Au_2Ag_8Cu_5$

Table S4. The mulliken charges analysis of Ag_9Cu_6.

Table S5. The crystal structure parameters for $[Au_2Ag_8Cu_5(C{\equiv}CBu^t)_{12}]SbF_6$.

Table S6. A summary of σ(Cu/Ag-C) and π (Au/Ag/Cu-C) bond lengths in motif 1, 2, 3, 4 and 5 of $Au_2Ag_8Cu_5$.

Table S7. A summary of σ and π bond lengths in motifs on the surface of Au_7Ag_8, Ag_9Cu_6 and $Au_2Ag_8Cu_5$.

Table S8. Lengths of bonds spread on different layer of $M_{core}@M_{cube}@M_{octahedron}$ structure in $Au_2Ag_8Cu_5$, Ag_9Cu_6, and Au_7Ag_8.

Table S9. Recovery of the Ag_9Cu_6 catalyst after CO_2RR test at applied potentials.

Table S10. Recovery of the $Au_2Ag_8Cu_5$ catalyst after CO_2RR test at applied potentials.

Table S11. The formate-selectivity comparison of recently reported atomically precise metal NCs in CO_2RR.

Table S12. The CO-selectivity comparison of recently reported atomically precise metal NCs in CO_2RR.

Table S13. Bader charges on the metal active atom bonded to *H.

Experimental Procedures

I. Synthesis.

Materials and Reagent: Dichloromethane (DCM), ethanol (EtOH), methanol (MeOH), acetonitrile (MeCN), diethyl ether, and ethyl acetate (EA) were purchased from Caiyunfei Chemical Reagents (Tianjin, China). 3, 3-dimethyl-1-butyne (^{t}BuC≡CH, 96%), triphenylphosphine (PPh_3, 98%), anhydrous dimethyl sulfide (Me_2S, 99.0%), anhydrous triethylamine (Et_3N, 99.5%), ammonium hydroxide ($NH_3{\cdot}H_2O$: 28.0 ~ 30.0% NH_3), silver oxide (Ag_2O, 99.0%), sodium hexafluoroantimonate(V) ($NaSbF_6$, 99.0%), copper (I) chloride (CuCl, 98%), and hydrogen tetrachloroaurate (III) trihydrate ($HAuCl_4{\cdot}3H_2O$, Au 50%) were acquired from Energy Chemicals (Shanghai, China). Sodium borohydride ($NaBH_4$, 98%) was obtained from Aladdin Industrial Corporation (Shanghai, China). The water with the resistivity of 18.3 $M\Omega{\cdot}cm^{-1}$ was supplied by a Barnstead Nanopure water system. All chemicals were used as received without further purification.

Synthesis of tert-butyl acetylene-protected trimetallic $Au_2Ag_8Cu_5$: Me_2SAuCl, $[Au_7Ag_8(C{\equiv}C\text{-}^tBu)_{12}]SbF_6$, and $[Ag_9Cu_6(C{\equiv}C\text{-}^tBu)_{12}]SbF_6$ were prepared by following the method in our previous reports.[1-2] For synthesizing $Au_2Ag_8Cu_5$ NCs, typically, 5 mg of $[Ag_9Cu_6(C{\equiv}C\text{-}^tBu)_{12}]SbF_6$ was first dissolved in 6 mL mixed solvents of DCM and MeOH (V_{DCM}: V_{MeOH} = 2: 1) under the ultrasound condition at room temperature (160 W, 40 kHz). Under vigorous stirring (1000 rpm), freshly prepared DCM solution (1 mL) containing 2 equivalents of Me_2SAuCl was added dropwise to the above solution for ca. 1 min in the absence of light. During the addition process, the reaction system changed from blue solution to violet suspension and then to bright red solution. The reaction mixture was kept stirring at room temperature for 1 h in the absence of light. After that, the light red solution was evaporated to give a black solid, which was successively washed with excess ethyl acetate and MeOH to remove the byproducts and inorganic salt, followed by extraction by DCM. The solution was centrifuged for 5 mins at 10000 $r{\cdot}min^{-1}$. The light red supernatant was subjected to evaporation in the dark at room temperature. Red block crystals were obtained after 1 week (yield: *ca.* 66.85% based on Cu). CCDC number is 2072663 for $[Au_2Ag_8Cu_5(C{\equiv}C\text{-}^tBu)_{12}]SbF_6$.

II. Measurements and instrumentation.

The surface chemical composition and valence state were examined by X-ray photoelectron spectroscopy (XPS, Phi X-tool instrument). Scanning electron microscopic (SEM) images and energy-dispersive X-ray spectroscopy (EDS) were collected with a field-emission scanning electron microscope (FESEM, Merlin). UV-visible (UV-Vis) absorption spectra were recorded on a Shimadzu 2600/2700 spectrophotometer (Japan). The liquid products were analyzed by using a Bruker AVANCE III 400 MHz nuclear magnetic resonance (NMR) instrument and phenol was added into the deuterated water as an internal standard. The electrochemical performance of the catalysts was evaluated on a CHI 710C electrochemical workstation.

III. Electrospray ionization mass spectrometry (ESI-MS)

The ESI-MS spectra were acquired on a Bruker UltiMate3000 time-of-flight (TOF) system. ESI-MS instrumental parameters were maintained at the following values: Capillary voltage, -3.5 kV; Dry temp, 200 °C; Nebulizer, 0.6 bar; Dry gas, 6.01 $mL{\cdot}min^{-1}$. The ESI sample was dissolved in dichloromethane (~1 $mg{\cdot}mL^{-1}$). All the mass spectra were obtained with positive ion mode. Calibration was performed using CsI clusters.

IV. X-ray Crystallography

The diffraction data was collected on an Agilent Technologies SuperNova Single Crystal Diffractometer using Cu K_α radiation (λ = 1.54178 Å) at 100 K. Absorption corrections were applied by using the program CrysAlis (multi-scan). Structure solution was carried out using SHELXT and refinement with SHELXL, within the OLEX2 graphical interface. All non-hydrogen atoms were refined first isotropically and then anisotropically. All the hydrogen atoms of the ligands were placed in calculated positions with fixed isotropic thermal parameters and included in the structure factor calculations in the final stage of full-matrix least-squares refinement. Detailed crystal data and structure refinements for the three compounds are given in **Table S5**. CCDC 2072663 for $[Au_2Ag_8Cu_5(C{\equiv}C\text{-}^tBu)_{12}]SbF_6$ contain the supplementary crystallographic data for this paper. These data are provided free of charge by the Cambridge Crystallographic Data Centre.

V. Computational details

All the spin-polarized density functional theory (DFT) calculations were implemented to investigate the electrocatalytic activity of M_{15} nanoclusters for CO_2 reduction in the Vienna ab initio simulation package (VASP5.4.4).[3] To save the computational cost, we simplified the $\text{-}C{\equiv}C\text{-}^tBu$ groups with $\text{-}C{\equiv}C\text{-}CH_3$ groups. These nanoclusters were placed in a cubic box with dimension of 22 Å × 22 Å × 22 Å, and their structures were optimized by the Perdew-Burke-Ernzerhof (PBE) function form of the generalized gradient approximation (GGA) to represent the interactions of electron exchange-correlation.[4] The ion-electron interaction was described with the projector augmented wave (PAW) method,[5] and the wave functions of all the computations were expanded via a plane-wave cutoff energy of 400 eV. The convergence criteria for energy and force was set as 10^{-5} eV and 0.02 $eV{\cdot}A^{-1}$ for maximal displacement, respectively. The Γ point only was used to sample the Brillouin zone, in addition, the van der Waals interactions between ligands were considered and described utilizing the empirical density functional dispersion (DFT-D3) method.[6] All atoms were unconstraint and fully relaxed during the simulation.

Based on the computational hydrogen electrode (CHE) model,[7] the change of Gibbs free energy for each CO_2RR elementary reaction can be calculated as:

$$\Delta G = \Delta E + \Delta E_{sol} + \Delta ZPE - T\Delta S \qquad \text{(S1)}$$

Where ΔE is the difference in the DFT total energy, ΔZPE is the difference of zero-point energy calculated from the vibrational frequencies, and ΔS is the entropy difference between the products and the reactants at 298.15 K. The ΔE_{sol} represents a solvation correction. For *COOH and *CO, the solvation correction is -0.25 eV and -0.1 eV, respectively.[8] For the gas molecules, the entropy is taken from NIST database. The zero-point energy and entropy correction at 298.15 K for various gas-phase species are provided in the following table.

Table. Zero-point energy (ZPE) and entropy correction (-T*S) for various gas-phase species at T=298.15 K.

Species	ZPE (eV)	-T*S (eV)
CO_2	0.31	-0.66
CO	0.13	-0.61
formate	0.90	-0.77
H_2	0.27	-0.40
H_2O	0.59	-0.58

For the adsorbed intermediates, only vibrational entropy is considered, which is calculated from the DFT calculated vibrational frequencies. In addition, due to the inaccurate description of CO_2 and CO molecules by PBE functional,[4, 9] we added correction of -0.34 eV for CO and +0.10 eV for CO_2.[10] H_2O and HCOOH are formed in the liquid phase. However, it is often difficult to calculate the free energy of the liquid phase using the standard DFT method. Therefore, we have corrected the DFT-calculated free energy of the gas phase, which is based on the free energy difference between the liquid and gas phase formations obtained in the NIST database:

$$G(H_2O,l) - G(H_2O,g) = -0.09\ eV \qquad \text{(S2)}$$

$$G(HCOOH,l) - G(HCOOH,g) = -0.12\ eV \qquad \text{(S3)}$$

Therefore, we used a correction of -0.09 eV and -0.12 eV for H_2O and HCOOH, respectively.

VI. Electrochemical measurements

To prepare the catalyst sample, the as-prepared M_{15} NC was loading on acidic multi-walled carbon (MWCNTs) with a mass ratio of 1 (5 mg NC and 5 mg MWCNTs). The catalyst ink was prepared by dispersing the sample in isopropyl alcohol (1.5 $mg \cdot mL^{-1}$) under sonication for 5 mins. Then, 1 mL catalyst suspension and 5 μL Nafion (5 wt.%) were uniformly mixed as the final catalyst ink. Subsequently, 50 μL catalytic ink was dropwise cast onto the carbon paper (2×1.5 cm^2) and dried at room temperature as the working electrode. 1 M KOH solution (pH= 14.0) was used as the electrolyte.

The electrochemical performance of the catalysts was evaluated on a CHI 710C electrochemical workstation. Linear sweep voltammetry (LSV) was conducted at a scan rate of 10 $mV \cdot s^{-1}$ from -0.39 to -1.19 V vs. RHE. The electrochemical performance of three catalysts on gas diffusion electrode (GDL, 2×1.5 cm^2) was carried out in a custom-designed flowcell reactor. The three NCs-coated carbon paper with a microporous layer (Sigracet 29 BCE, Fuel Cell Store) was applied as the GDL cathode. Ag/AgCl in 1.0 M KCl saturated aqueous electrolyte was employed as the reference electrode. The catholyte and anolyte chambers were separated by an anion exchange membrane (SELEMION, 2×1.5 cm^2). During the measurements, the flow rate of CO_2 into the cathode GDL was 20 $mL \cdot min^{-1}$ and flow rate of the catholyte (1 M KOH) were controlled to be 65 rpm via a peristaltic pump (Cole-Parmer).

Electrode potentials measured on the Ag/AgCl scale ($E_{Ag/AgCl}$) were converted into the reversible hydrogen electrode (RHE) scale using the following equation:

$$E_{RHE} = E_{Ag/AgCl} + 0.1976 + 0.0591\, pH \tag{S3}$$

The output of the gas flow from the cathode chamber was directed into a gas chromatograph instrument (GC, Huaai 9560) for on-line identification and quantification of the gaseous products, which was purged for 30 mins prior to the test. The liquid products were analyzed by using a Bruker AVANCE III 400 MHz NMR instrument and phenol was added into the deuterated water as an internal standard.

The faradaic efficiency (FE_X) and partial current density (j_X) of X (X= CO or H_2 or formate) were calculated as below:

$$Gas\ products: FE_{X,\ G} = \frac{Q_i}{Q_t} = \frac{I_i}{I_t} = \frac{(V_i \times v \times n \times F)}{I_t} \tag{S4}$$

$$Liquid\ products: FE_{X,L} = \frac{Q_i}{Q_t} = \frac{(N_i \times n \times F)}{Q_t} \tag{S5}$$

$$j_X = \frac{FE_X \times C}{t \times Area} \tag{S6}$$

where Q_t stands for the total charge consumed, Q_i represents the charge reducing a certain product, I_t stands for the current value output from electrochemical workstation, I_i represents the partial current reducing a certain product, V_i is volume fraction of the product measured by GC, v is the flow rate of CO_2, N_i is the amount of moles of the product measured by NMR, n is the number of electrons transferred in the elementary reaction (which is 2 for CO, H_2, and formate), and F denotes the Faradaic constant (96485 $C \cdot mol^{-1}$), C is total charge consumed in electrochemical reaction, t is reaction time (s), Area is geometry area of the electrode (cm^2).

References

(1) Ma, X.; Tang, Z.; Qin, L.; Peng, J.; Li, L.; Chen, S., *Nanoscale* **2020,** *12*, 2980-2986.

(2) Ma, X.; Xiong, L.; Qin, L.; Tang, Y.; Ma, G.; Pei, Y.; Tang, Z., *Chem. Sci.* **2021,** *12*, 12819-12826.

(3) Kresse, G.; Furthmuller, J., *Phys. Rev. B: Condens. Matter* **1996,** *54*, 11169-11186.

(4) Perdew, J. P.; Burke, K.; Ernzerhof, M., . *Phys. Rev. Lett.* **1996,** *77*, 3865-3868.

(5) Blochl, P. E., *Phys. Rev. B: Condens. Matter* **1994,** *50*, 17953-17979.

(6) Garzon, I. L.; PosadaAmarillas, A., *Phys. Rev. B* **1996,** *54*, 11796-11802.

(7) Norskov, J. K.; Rossmeisl, J.; Logadottir, A.; Lindqvist, L.; Kitchin, J. R.; Bligaard, T.; Jonsson, H., *J. Phys. Chem. B* **2004,** *108*, 17886-17892.

(8) Ouyang, Y.; Shi, L.; Bai, X.; Li, Q.; Wang, J., *Chem. Sci.* **2020,** *11*, 1807-1813.

(9) Peterson, A. A.; Abild-Pedersen, F.; Studt, F.; Rossmeisl, J.; Norskov, J. K., *Energy Environ. Sci.* **2010,** *3*, 1311-1315.

(10) Tang, Q.; Lee, Y.; Li, D.-Y.; Choi, W.; Liu, C. W.; Lee, D.; Jiang, D.-e., *J. Am. Chem. Soc.* **2017,** *139*, 9728-9736.

(11) Sun, Y. N.; Liu, X.; Xiao, K.; Zhu, Y.; Chen, M. Y., *ACS Catal.* **2021,** *11*, 11551-11560.

(12) Tang, Q.; Lee, Y.; Li, D. Y.; Choi, W.; Liu, C. W.; Lee, D.; Jiang, D. E., *J. Am. Chem. Soc.* **2017,** *139*, 9728-9736.

(13) Qin, L.; Sun, F.; Ma, X.; Ma, G.; Tang, Y.; Wang, L.; Tang, Q.; Jin, R.; Tang, Z., *Angew. Chem. Int. Ed.* **2021,** *60*, 26136-26141.

(14) Yuan, S. F.; He, R. L.; Han, X. S.; Wang, J. Q.; Guan, Z. J.; Wang, Q. M., *Angew. Chem. Int. Ed.* **2021,** *60*, 14345-14349.

(15) Wan, X. K.; Wang, J. Q.; Wang, Q. M., *Angew. Chem. Int. Ed.* **2021,** *60*, 20748-20753.

(16) Li, S.; Nagarajan, A. V.; Li, Y.; Kauffman, D. R.; Mpourmpakis, G.; Jin, R., *Nanoscale* **2021,** *13*, 2333-2337.

(17) Seong, H.; Efremov, V.; Park, G.; Kim, H.; Yoo, J. S.; Lee, D., *Angew. Chem. Int. Ed.* **2021,** *60*, 14563-14570.

(18) Li, S.; Nagarajan, A. V.; Alfonso, D. R.; Sun, M.; Kauffman, D. R.; Mpourmpakis, G.; Jin, R., *Angew. Chem. Int. Ed.* **2021,** *60*, 6351-6356.

(19) Zhuang, S.; Chen, D.; Liao, L.; Zhao, Y.; Xia, N.; Zhang, W.; Wang, C.; Yang, J.; Wu, Z., *Angew. Chem. Int. Ed.* **2020,** *59*, 3073-3077.

(20) Lin, X.; Ma, W.; Sun, K.; Sun, B.; Fu, X.; Ren, X.; Liu, C.; Huang, J., *J. Phys. Chem. Lett.* **2020,** *12*, 552-557.

(21) Li, S.; Alfonso, D.; Nagarajan, A. V.; House, S. D.; Yang, J. C.; Kauffman, D. R.; Mpourmpakis, G.; Jin, R., *ACS Catal.* **2020,** *10*, 12011-12016.

(22) Zhao, S.; Austin, N.; Li, M.; Song, Y. B.; House, S. D.; Bernhard, S.; Yang, J. C.; Mpourmpakis, G.; Jin, R. C., *ACS Catal.* **2018,** *8*, 4996-5001.

(23) Xu, J. Y.; Xiong, L.; Cai, X.; Tang, S. S.; Tang, A. C.; Liu, X.; Pei, Y.; Zhu, Y., *Chem. Sci.* **2022,** *13*, 2778-2782.

(24) Gao, Z.-H.; Wei, K.; Wu, T.; Dong, J.; Jiang, D.-e.; Sun, S.; Wang, L.-S., *J. Am. Chem. Soc.* **2022,** *144*, 5258-5262.

Supporting Figures

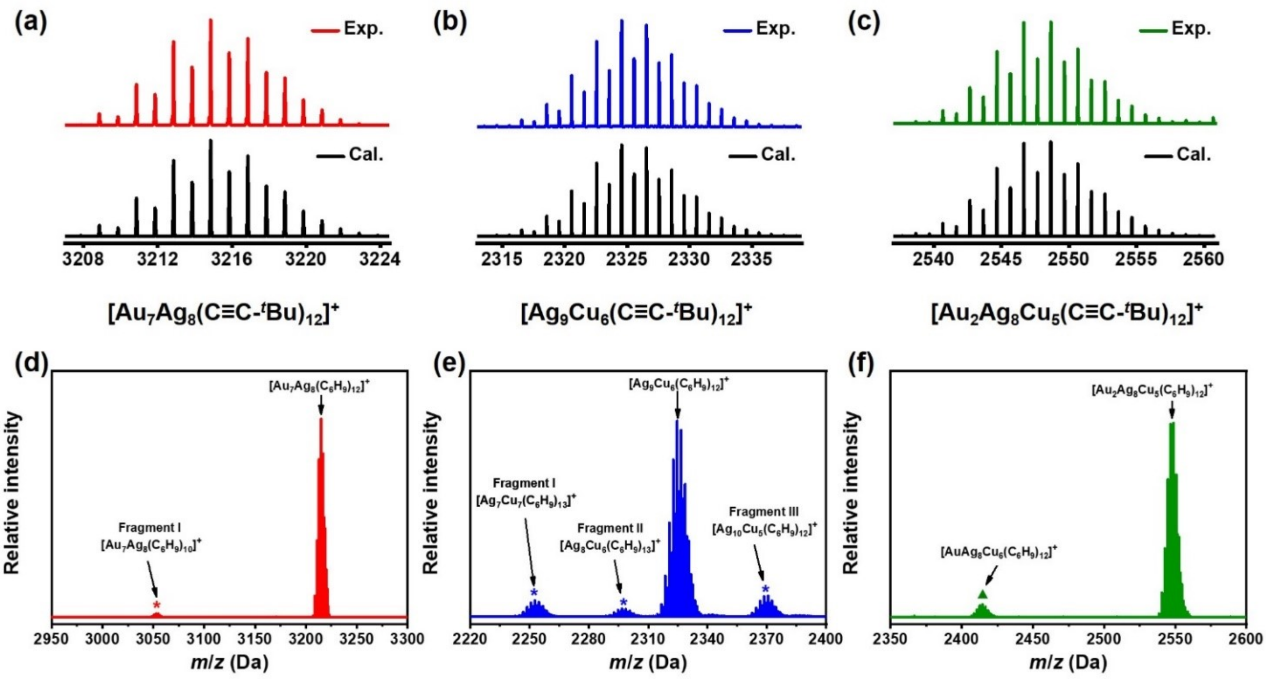

Figure S1. ESI-MS spectra of $[Au_7Ag_8(C\equiv C\text{-}{}^tBu)_{12}]^+$ (red), $[Ag_9Cu_6(C\equiv C\text{-}{}^tBu)_{12}]^+$ (blue) and $[Au_2Ag_8Cu_5(C\equiv C\text{-}{}^tBu)_{12}]^+$ (green) in positive mode. The experimental isotopic patterns and simulated (black) data of (a) Au_7Ag_8, (b) Ag_9Cu_6 and (c) $Au_2Ag_8Cu_5$ NCs. The local enlarged view of ESI-MS spectra of (d) Au_7Ag_8 (from 2950 to 3300 Da), (e) Ag_9Cu_6 (from 2220 to 2400 Da) and (f) $Au_2Ag_8Cu_5$ (from 2350 to 2550 Da). The asterisks (*) indicate the fragments of Au_7Ag_8 and Ag_9Cu_6 NCs, and the triangle (▲) indicates the product exchanged by one Au atom.

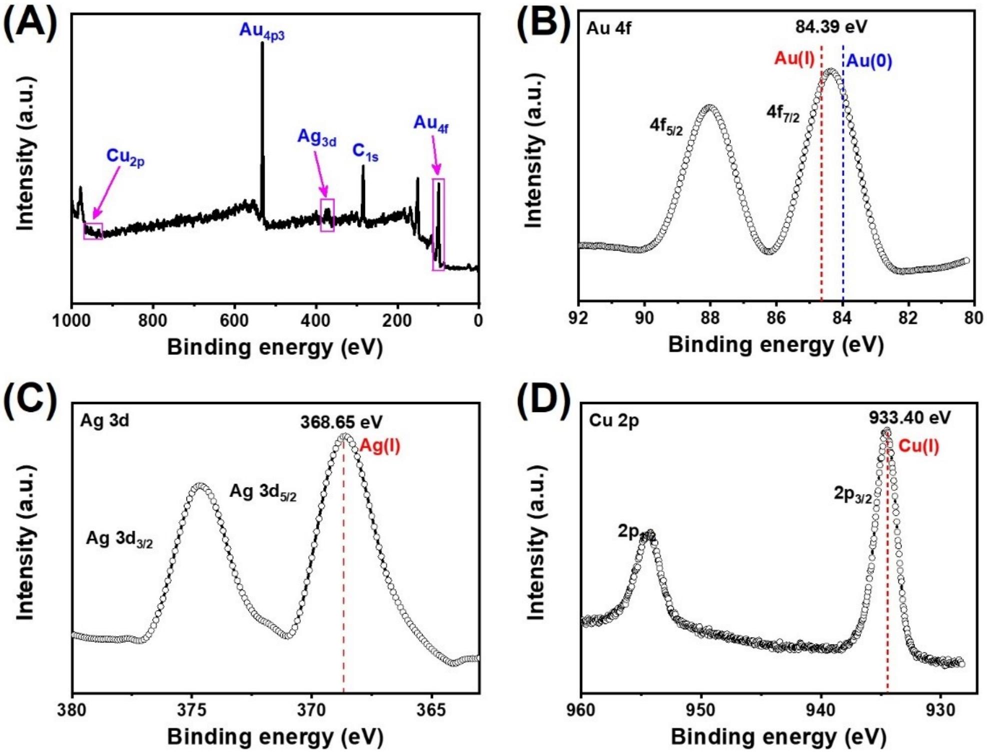

Figure S2. (a) XPS survey scan spectra of $Au_2Ag_8Cu_5$ NC. The core-level XPS spectra of the (b) Au 4f, (c) Ag 3d and (d) Cu 2p electrons in $Au_2Ag_8Cu_5$ NC. The binding energy was calibrated based on C 1s peak at 284.5 eV.

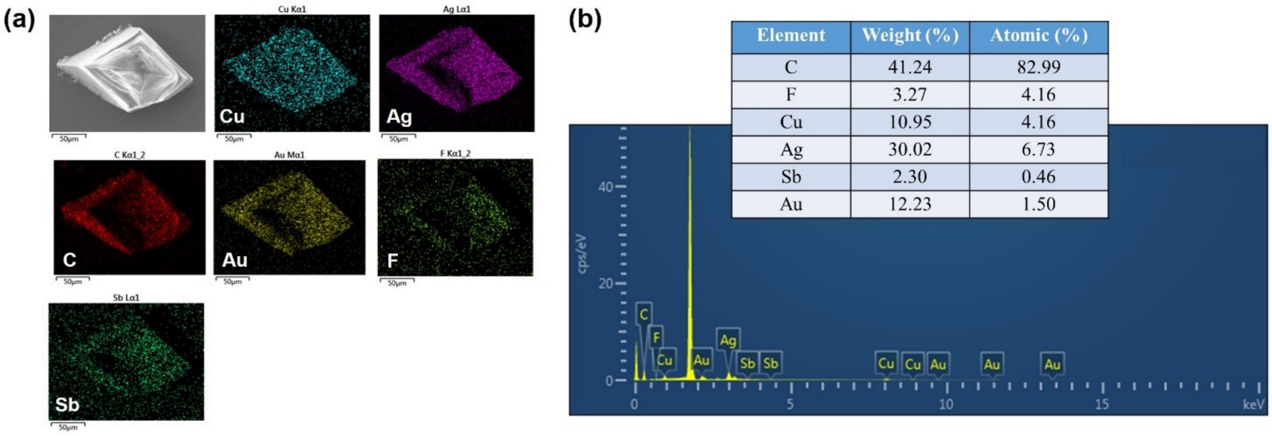

Element	Weight (%)	Atomic (%)
C	41.24	82.99
F	3.27	4.16
Cu	10.95	4.16
Ag	30.02	6.73
Sb	2.30	0.46
Au	12.23	1.50

Figure S3. (a) SEM image and the corresponding elemental maps of the $Au_2Ag_8Cu_5$ crystal. (b) EDS spectrum of $Au_2Ag_8Cu_5$ and the inserted table displays the elemental percentage of Cu, Ag, Au, Sb, C, and F in $Au_2Ag_8Cu_5$ NCs.

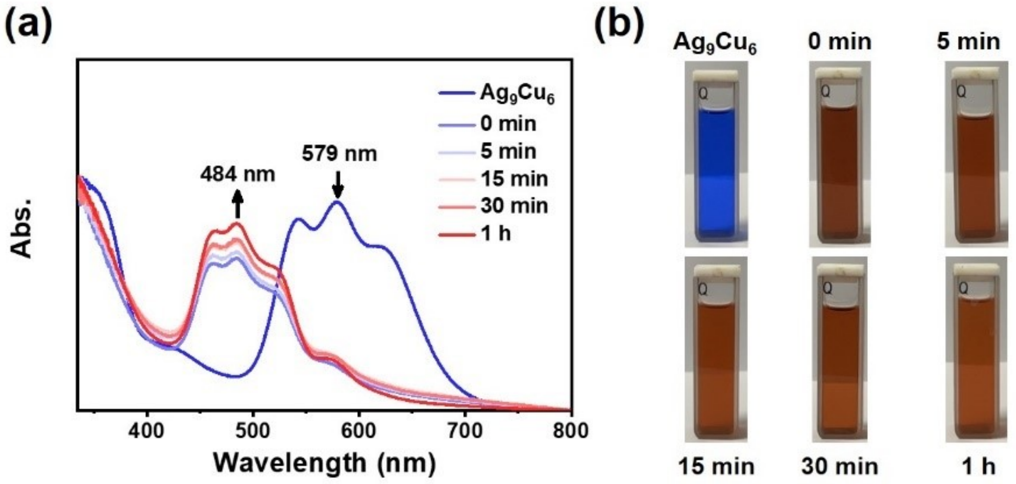

Figure S4. The in-situ monitoring of the content change during the formation process of $Au_2Ag_8Cu_5$ NC. (a) Time resolved UV-vis absorbance spectra (from Ag_9Cu_6 to the reaction mixture at 1 h after adding $Me_2SAu(I)Cl$), (b) The reaction solution with digital photos.

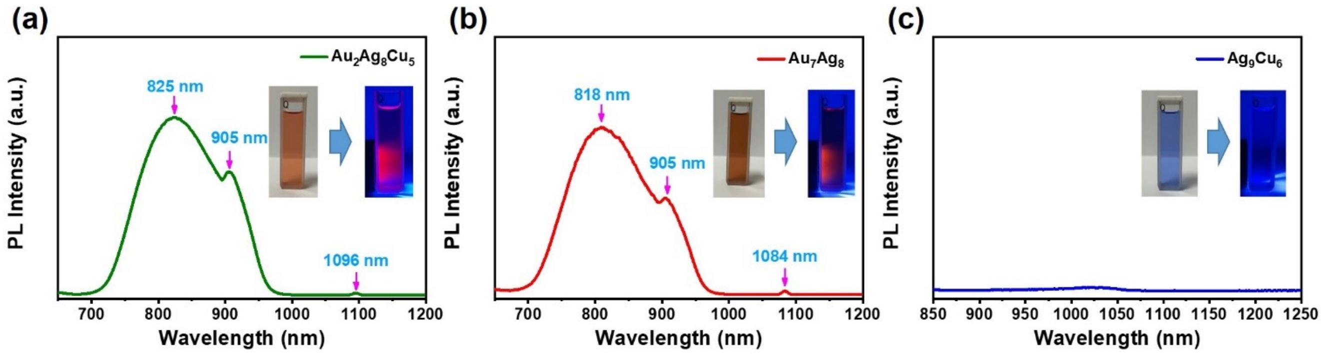

Figure S5. The emission spectra of $Au_2Ag_8Cu_5$ (λ_{ex}= 490 nm), Au_7Ag_8 (λ_{ex}= 482 nm) and Ag_9Cu_6 (λ_{ex}= 580 nm) NCs in dichloromethane. Inset: photographs of the three NCs in dichloromethane under room light (left) and 365 nm UV-light (right), respectively.

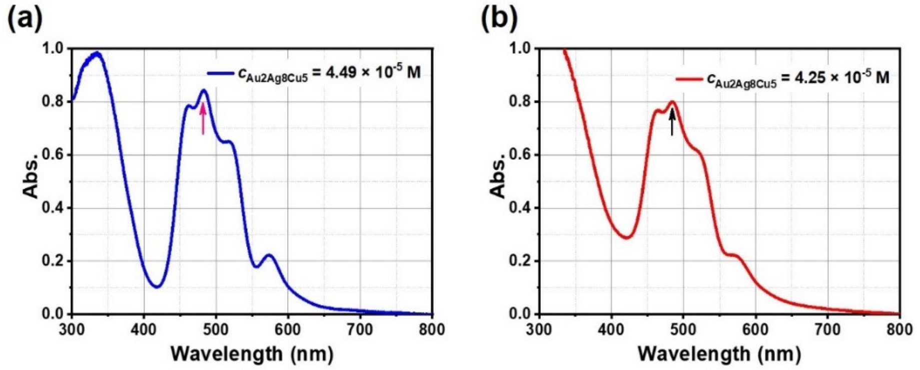

Figure S6. (a) The standard absorbance curve of the isolated $Au_2Ag_8Cu_5$ NC, and (b) Absorbance spectrum of its reaction mixture at 1 h.

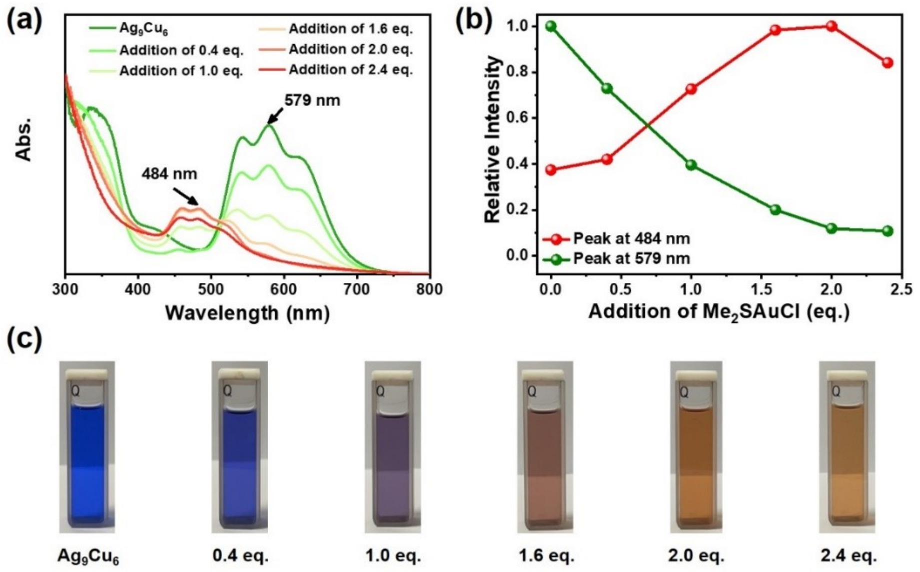

Figure S7. (a) Absorbance spectra of the metal exchange reaction for 1 h with different amounts (from 0 to 2.4 eq. per Ag_9Cu_6) of $Me_2SAu(I)Cl$. (b) The change of relative absorbance intensity of peaks (for Ag_9Cu_6, 579 nm; for $Au_2Ag_8Cu_5$, 484 nm). (c) Digital photos of the reaction mixture with different $Me_2SAu(I)Cl$ amounts.

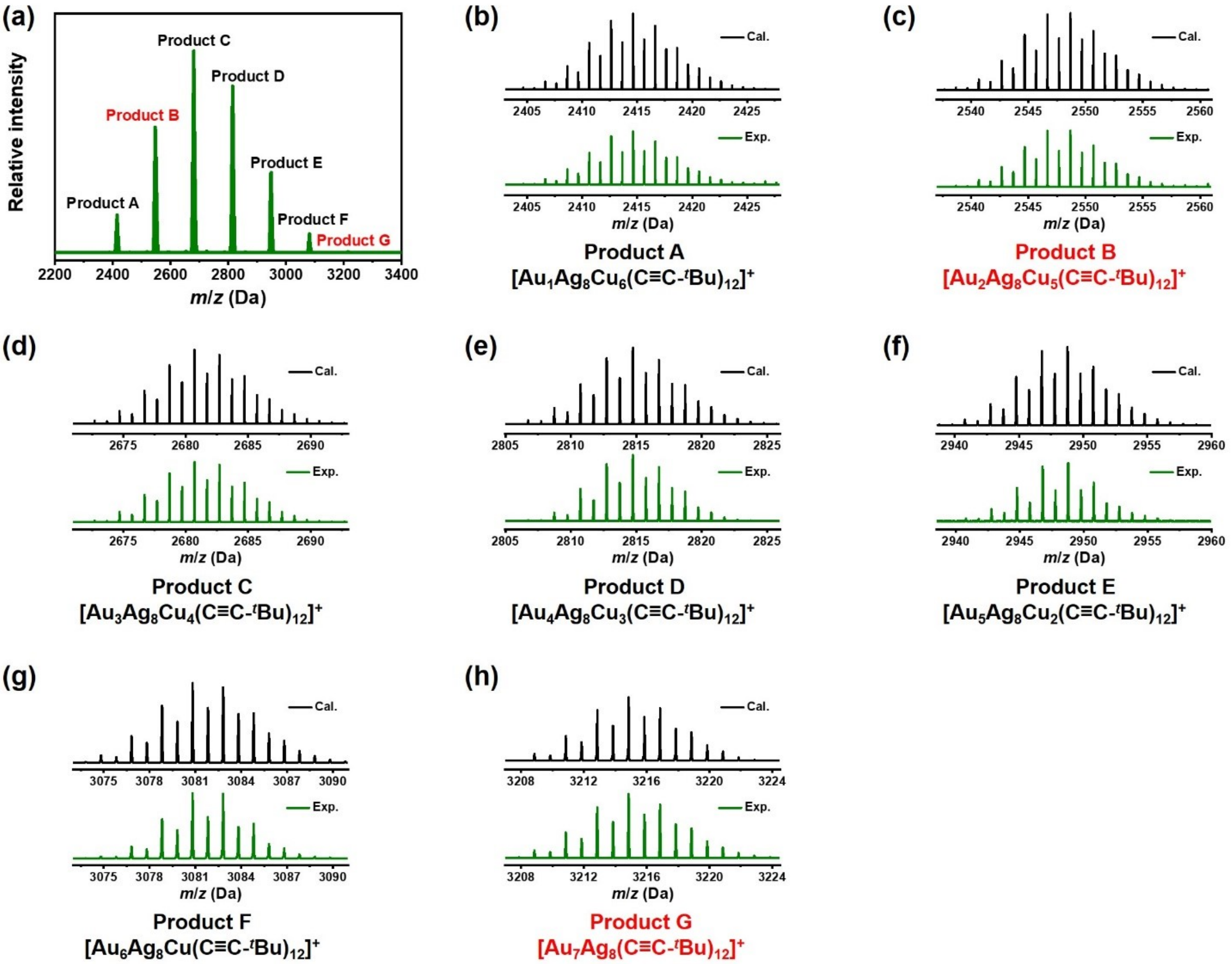

Product A $[Au_1Ag_8Cu_6(C≡C\text{-}{}^tBu)_{12}]^+$

Product B $[Au_2Ag_8Cu_5(C≡C\text{-}{}^tBu)_{12}]^+$

Product C $[Au_3Ag_8Cu_4(C≡C\text{-}{}^tBu)_{12}]^+$

Product D $[Au_4Ag_8Cu_3(C≡C\text{-}{}^tBu)_{12}]^+$

Product E $[Au_5Ag_8Cu_2(C≡C\text{-}{}^tBu)_{12}]^+$

Product F $[Au_6Ag_8Cu(C≡C\text{-}{}^tBu)_{12}]^+$

Product G $[Au_7Ag_8(C≡C\text{-}{}^tBu)_{12}]^+$

Figure S8. (a) Positive-mode ESI-MS spectra of the reaction for 1 h under the addition (8 eq. per Ag_9Cu_6) of $Me_2SAu(I)Cl$. The experimental isotopic patterns and simulated (black) data of (b to h) molecular ion peak of product A to G.

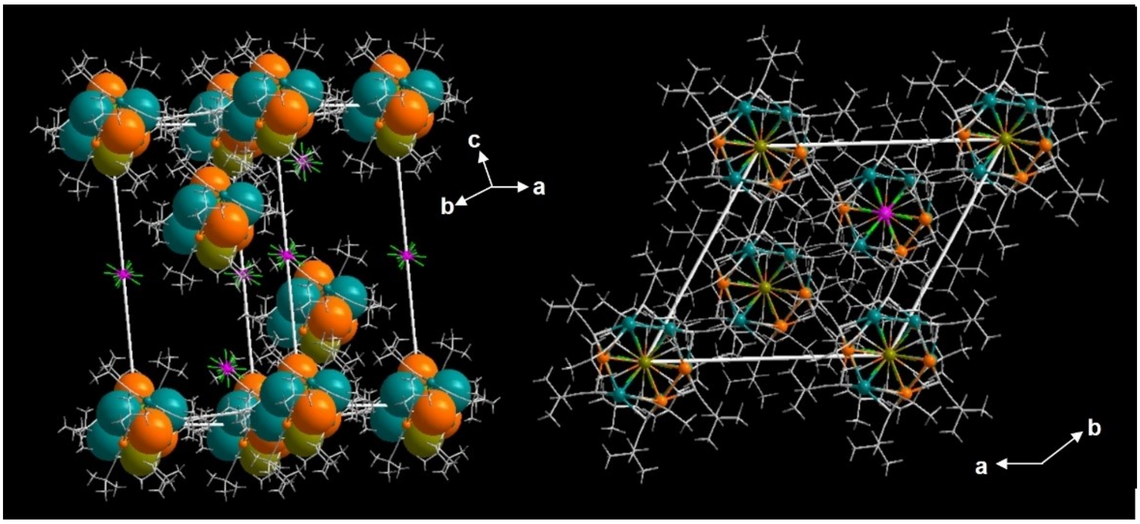

Figure S9. The crystal packing diagram of $Au_2Ag_8Cu_5$. Color labels: yellow, Au atoms; cyan, Ag atoms; orange, Cu atoms; purple, Sb atoms; green, F atoms; gray, C atoms; white, H atoms.

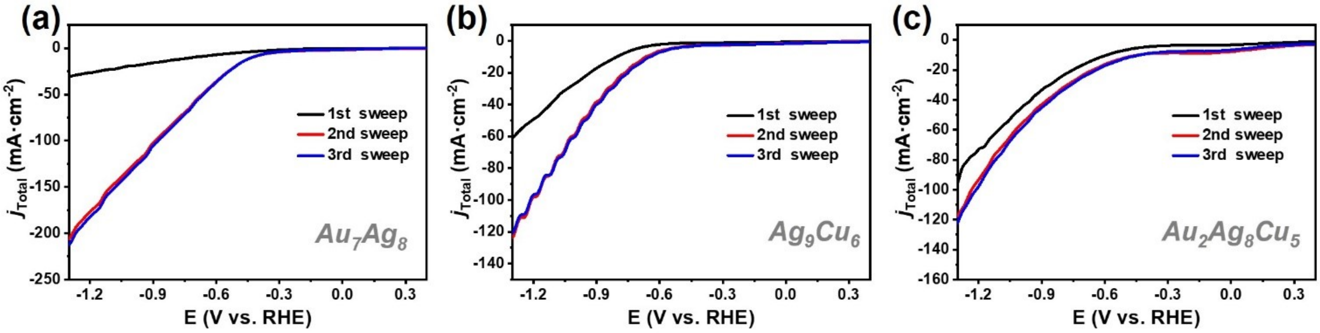

Figure S10. LSV curves recorded during the first (black), second (red) and third (blue) sweeps on (a) Au_7Ag_8/GDL, (b) Ag_9Cu_6/GDL, and (c) $Au_2Ag_8Cu_5$/GDL in 1.0 M KOH electrolyte at 50 mV·s^{-1}.

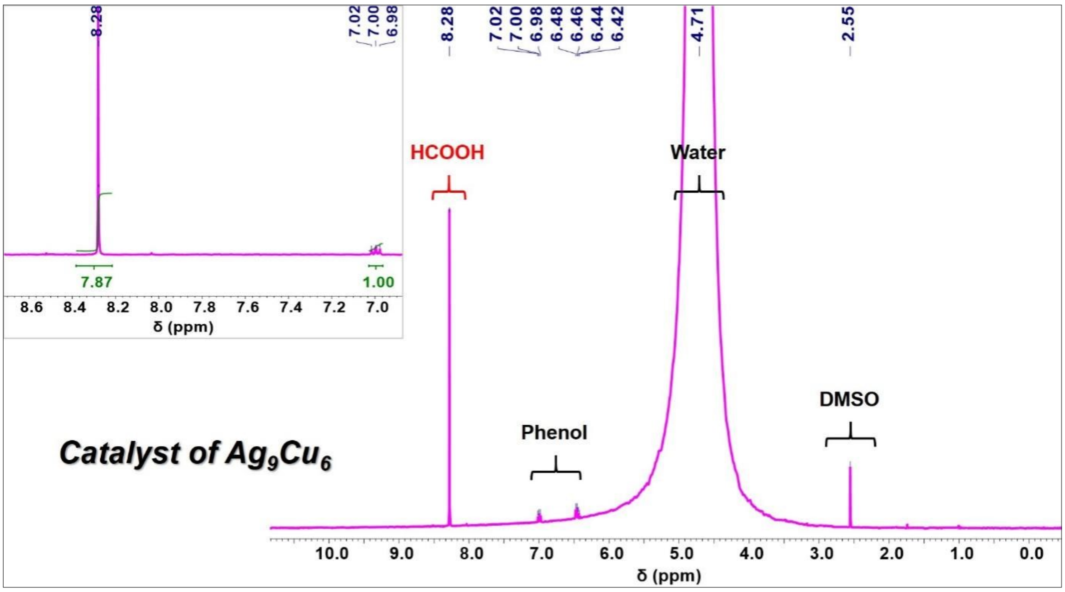

Figure S11. The ^{1}H-NMR spectra of the product in liquid phase for Ag_9Cu_6/GDL. Inset: Zoomed-in region is the ^{1}H-NMR spectra, which confirms the formate production.

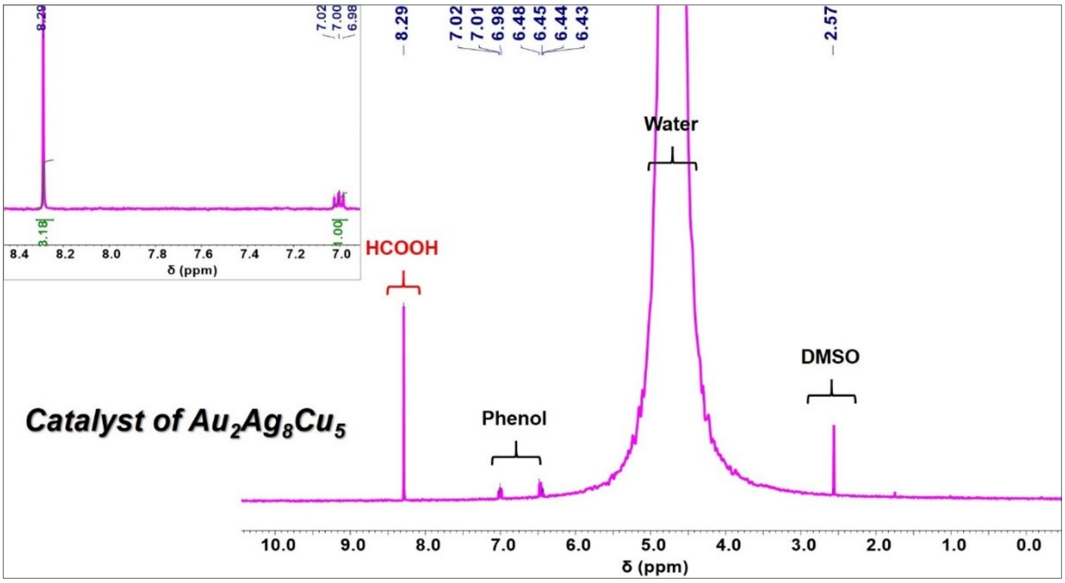

Figure S12. The ^{1}H-NMR spectra of the product in liquid phase for $Au_2Ag_8Cu_5$/GDL. Inset: Zoomed-in region is the ^{1}H-NMR spectra, which confirms the formate production.

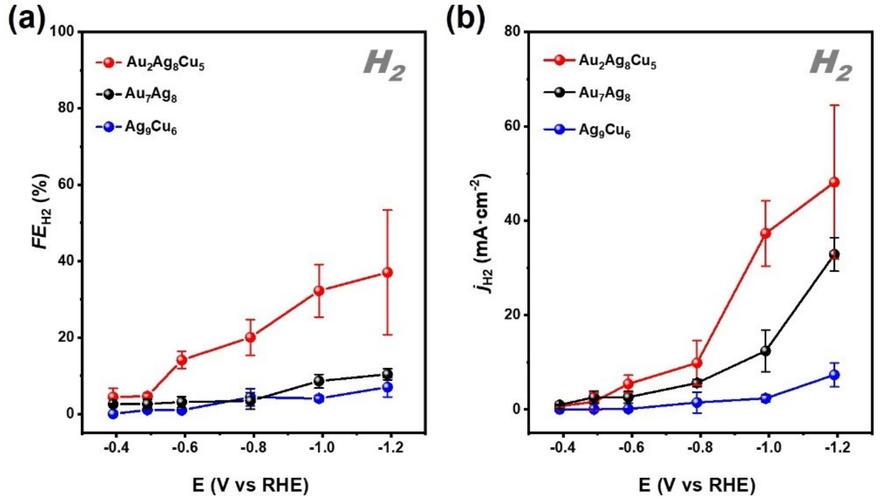

Figure S13. H_2 (a) faradaic efficiency and (b) the corresponding partial current density for the three NC/GDLs examined at different applied potentials.

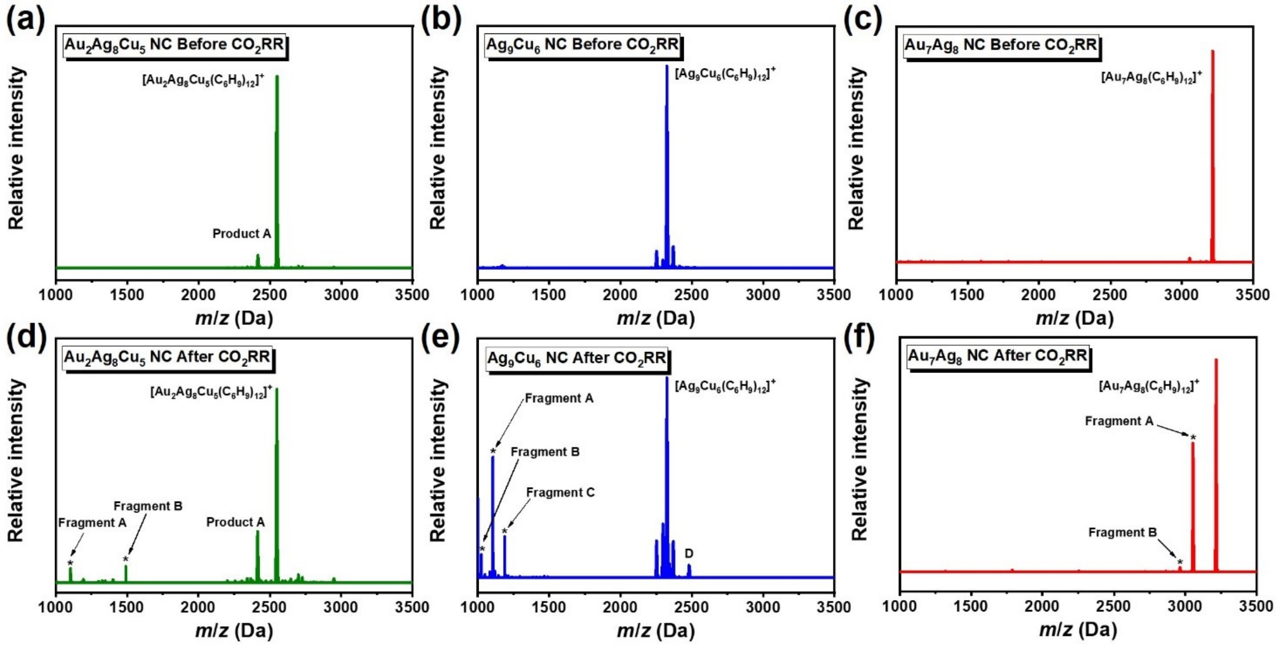

Figure S14. Positive-mode ESI-MS spectra of (a, d) $Au_2Ag_8Cu_5$, (b, e) Ag_9Cu_6 and (c, f) Au_7Ag_8 NCs before and after CO_2RR.

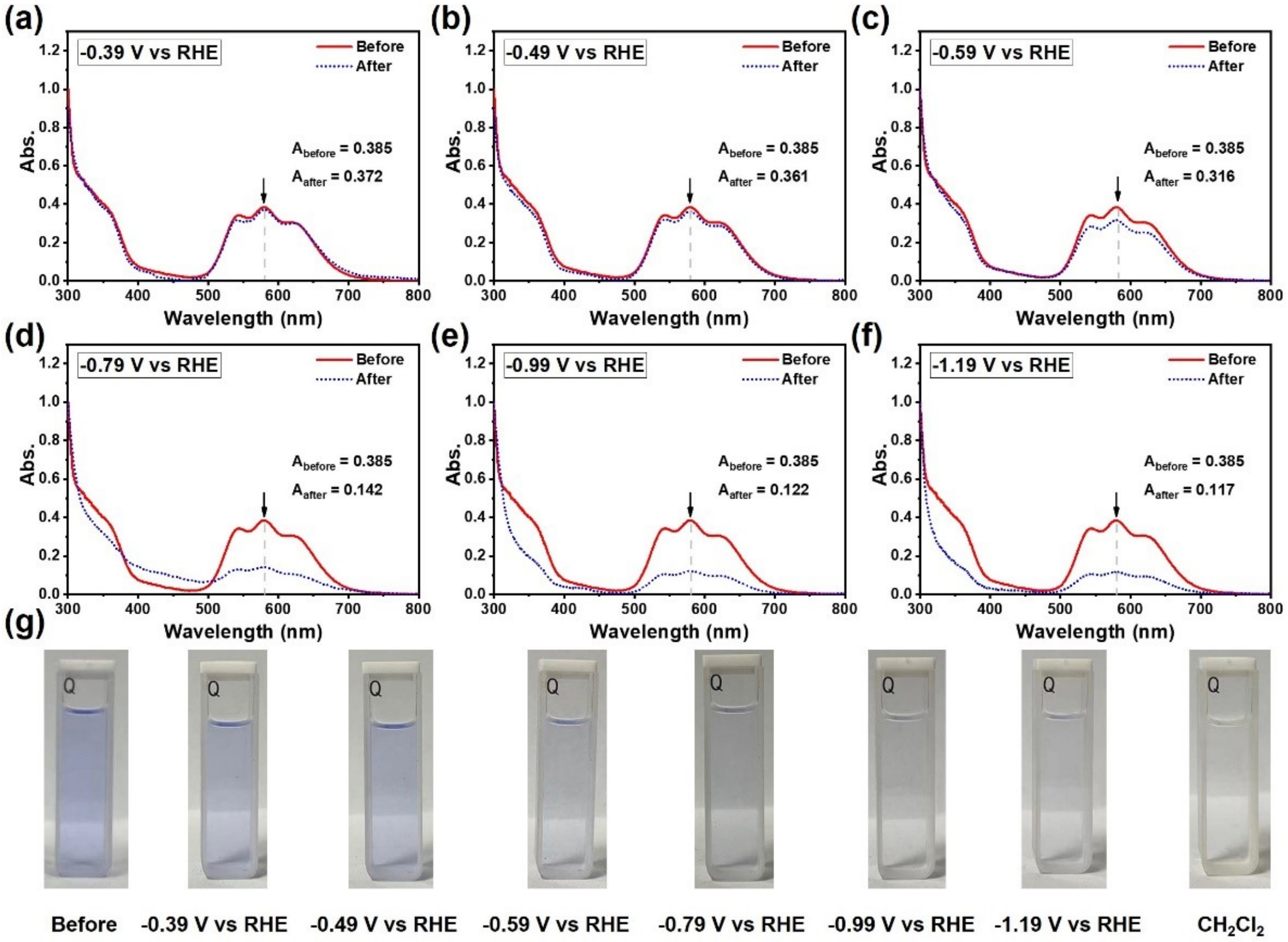

Figure S15. (a to f) Absorbance spectra of the Ag_9Cu_6/GDL before and after CO_2RR test at applied potentials, (g) corresponding photos of the dichloromethane solution.

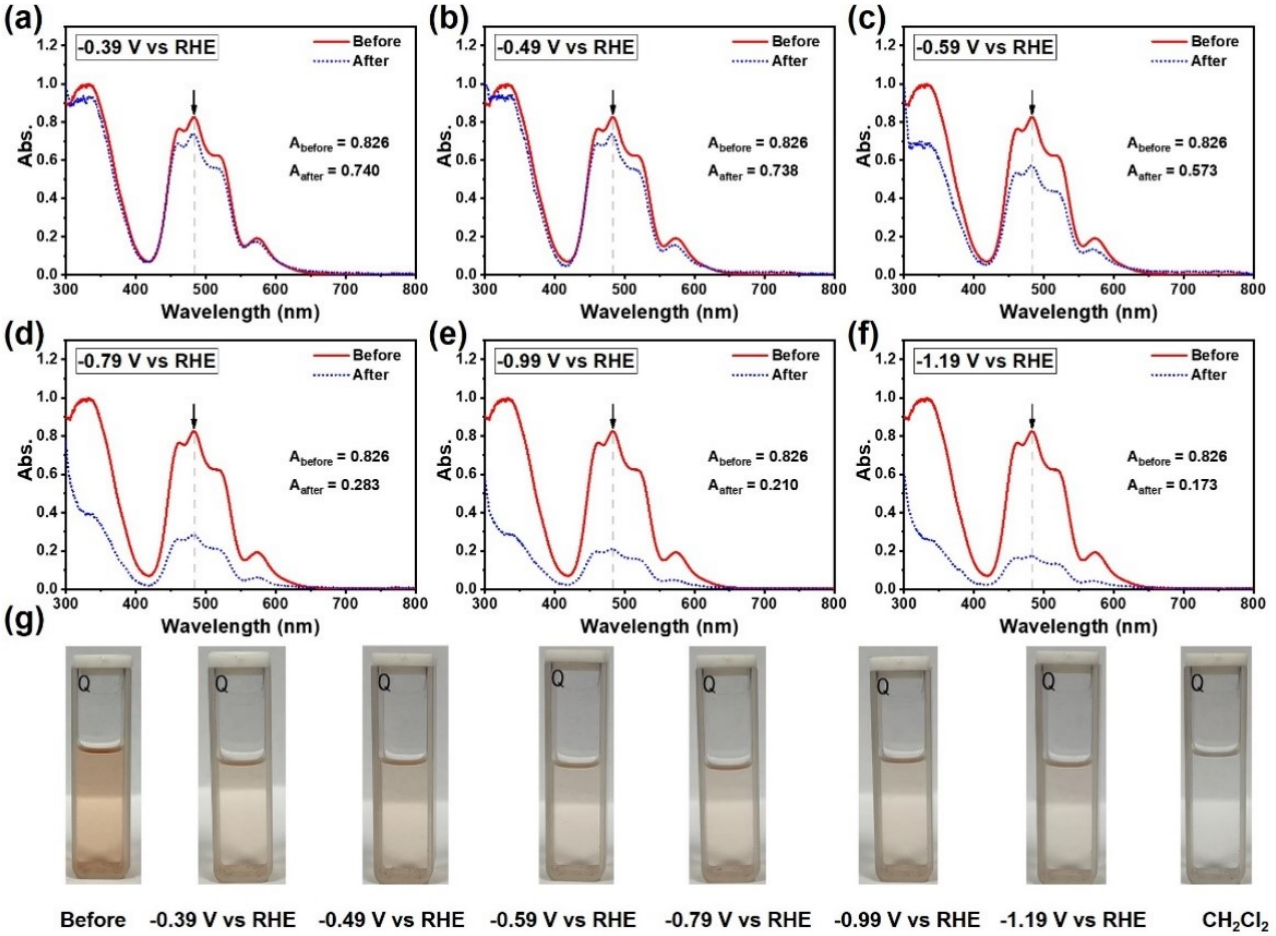

Figure S16. (a to f) Absorbance spectra of the $Au_2Ag_8Cu_5$/GDL before and after CO_2RR test at applied potentials, (g) the corresponding photos of the dichloromethane solution.

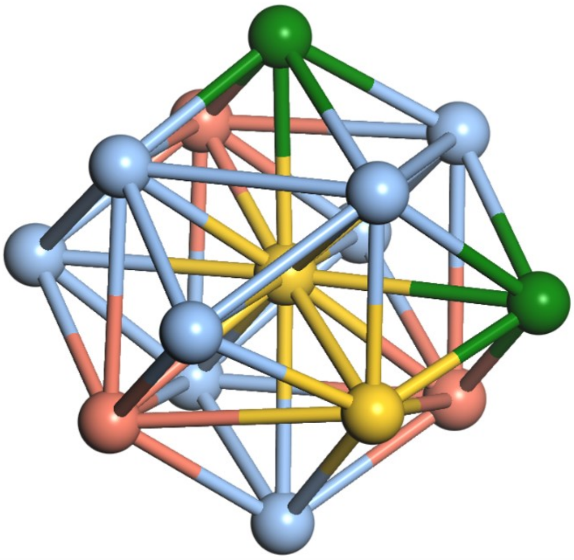

$Au@AuAg_4Cu_3@Ag_4Cu_2$

Figure S17. The detailed core-shell-shell configuration ($M_{core}@M_{cube}@M_{octahedron}$) of $Au@AuAg_4Cu_3@Ag_4Cu_2$ (-C≡C-CH_3 groups omitted for clarity).

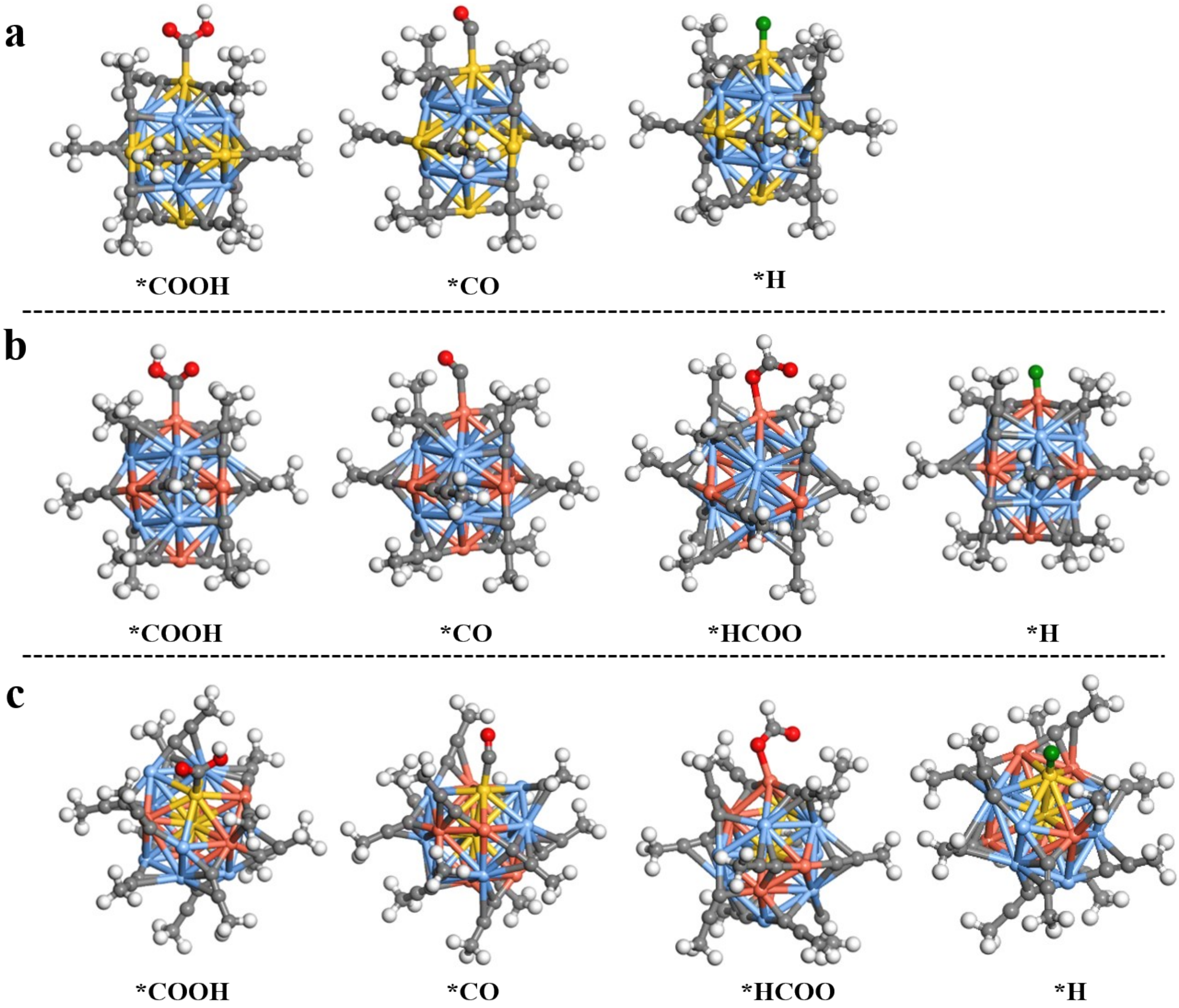

Figure S18. Schematic presentation of adsorption structures of *COOH, *CO, *HCOO, and *H intermediates on (a) $[Au_7Ag_8(C{\equiv}C\text{-}CH_3)_{12}]^+$, (b) $[Ag_9Cu_6(C{\equiv}C\text{-}CH_3)_{12}]^+$, and (c) $[Au_2Ag_8Cu_5(C{\equiv}C\text{-}CH_3)_{12}]^+$ NCs, respectively. Color legend: Au, gold; Ag, blue; Cu, brick-red; C, gray; O, red; *H, green; other H, white.

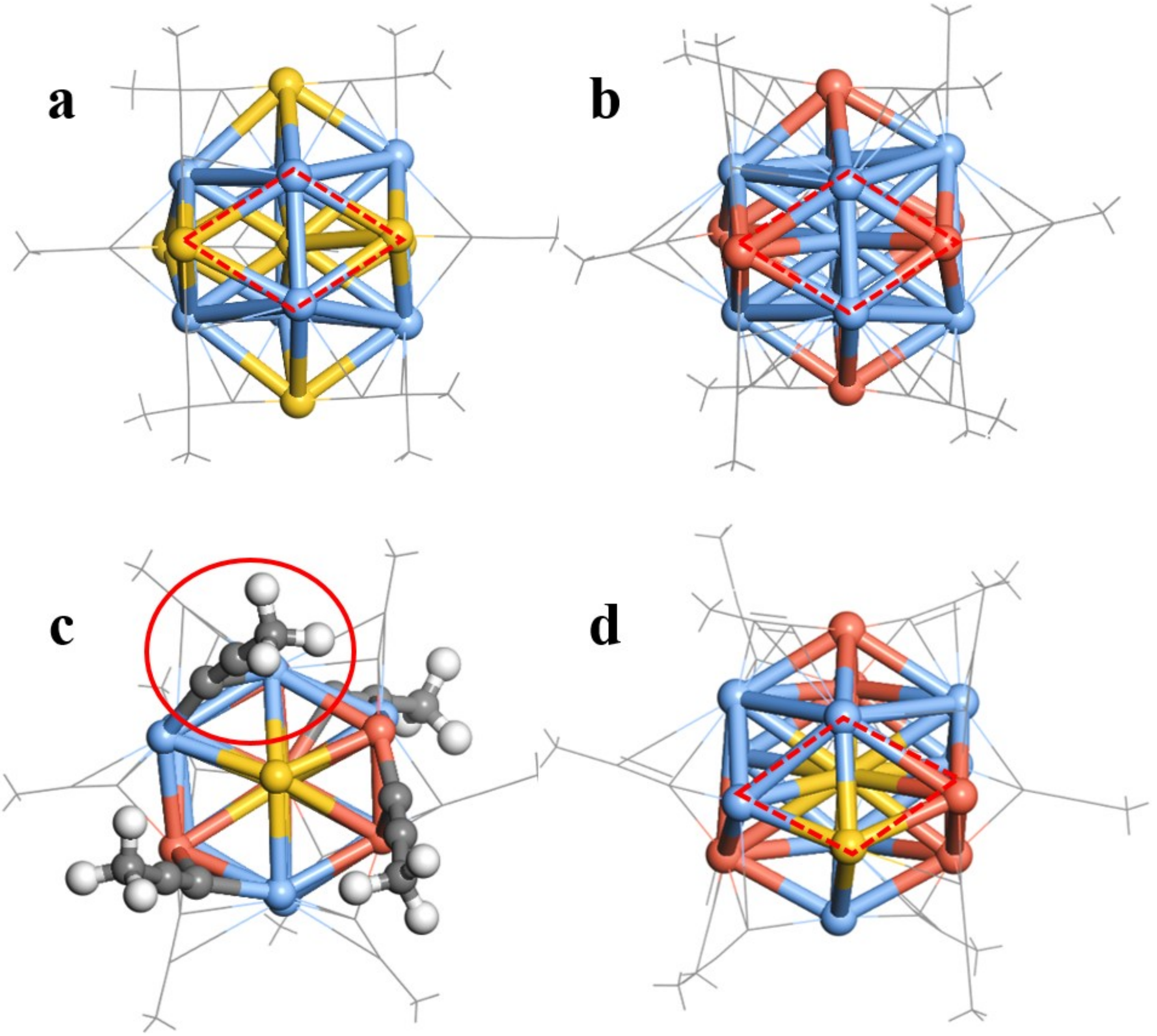

Figure S19. The exposed 111-like surface (red dotted line) after releasing one -C≡C-CH_3 ligand from (a) $[Au_7Ag_8(C≡C\text{-}CH_3)_{12}]^+$, (b) $[Ag_9Cu_6(C≡C\text{-}CH_3)_{12}]^+$, and (d) $[Au_2Ag_8Cu_5(C≡C\text{-}CH_3)_{12}]^+$ NCs. (c) Highlight four unique ligand removal sites attached to the core of $Au_2Ag_8Cu_5^+$, and the most favorable site for removal is circled in red. Color legend: Au, gold; Ag, blue; Cu, brick-red; C, gray; H, white.

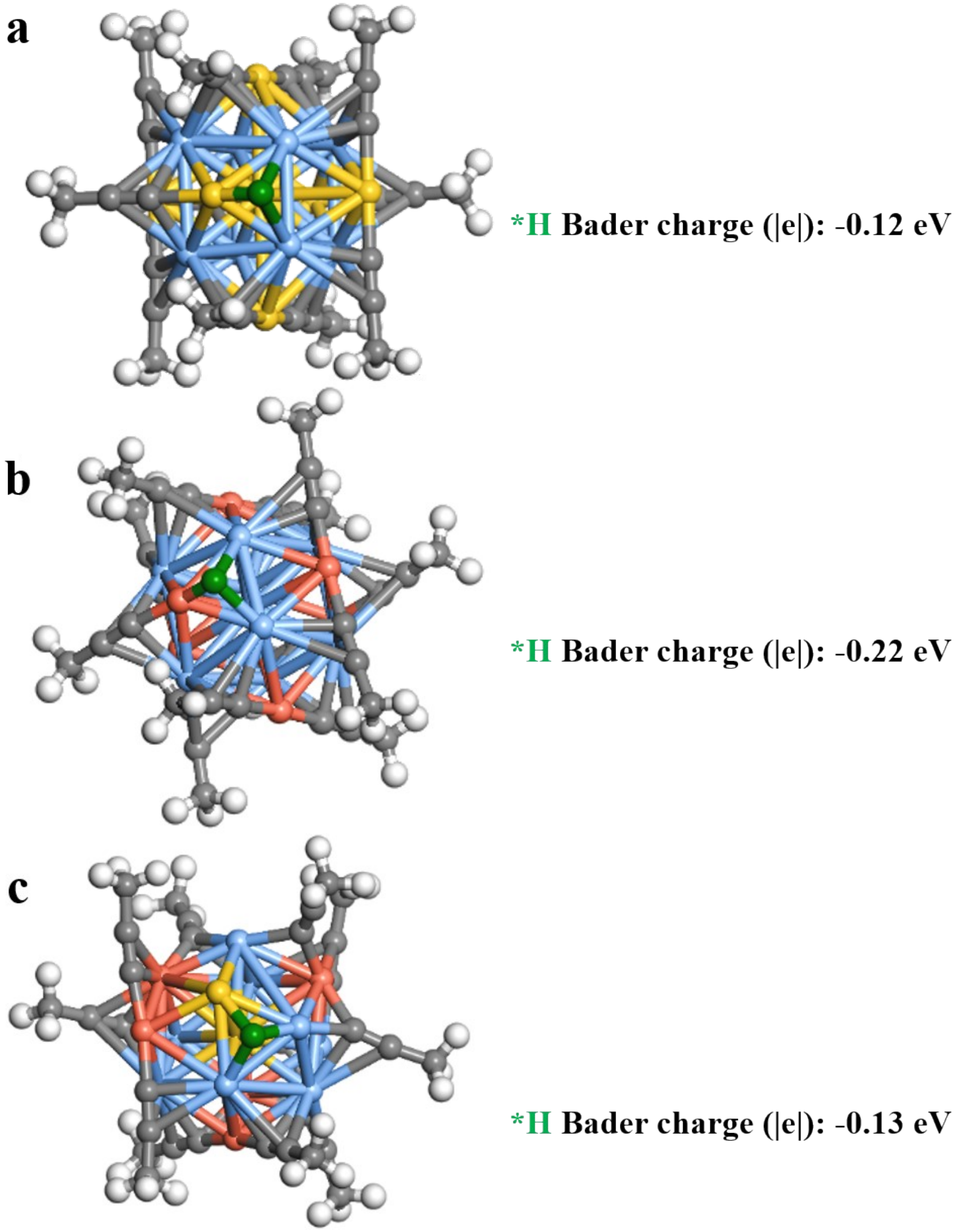

Figure S20. Adsorption structure of *H intermediate on the (a) $[Au_7Ag_8(C≡C\text{-}CH_3)_{11}]^+$, (b) $[Ag_9Cu_6(C≡C\text{-}CH_3)_{11}]^+$, and (c) $[Au_2Ag_8Cu_5(C≡C\text{-}CH_3)_{11}]^+$ NCs. The Bader charge of the corresponding *H atom is given on the right. Color legend: Au, gold; Ag, blue; Cu, brick-red; C, gray; O, red; *H, green; other H, white.

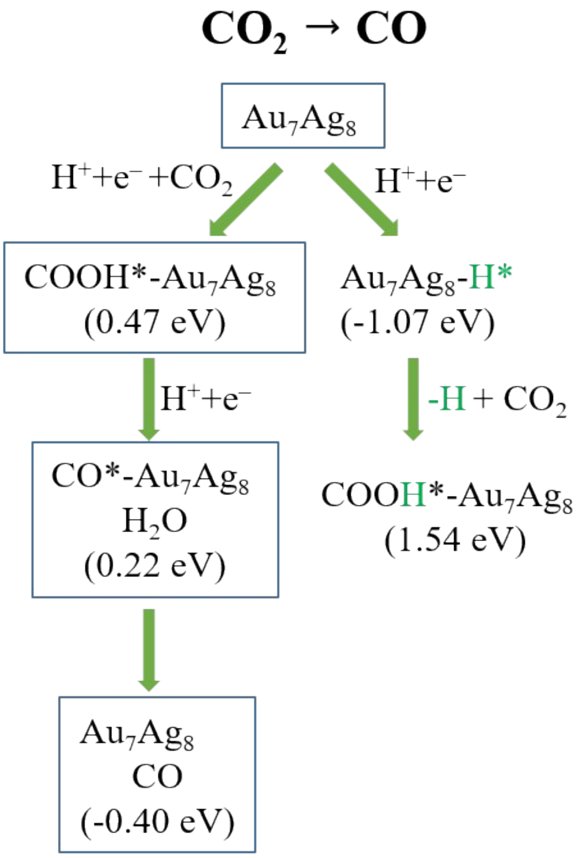

Figure S21. Reaction scheme for CO_2 electroreduction on $[Au_7Ag_8(C{\equiv}C\text{-}CH_3)_{11}]^+$ to form CO. The calculated free energy difference (ΔG) for each elementary step is shown under each intermediate state. The most favorable reaction pathway is highlighted with the blue box. Of note, the first surface hydride transfer to produce COOH* is more difficult than direct protonation reduction, so subsequent reactions from COOH* to CO through hydride channel can be disregarded. The same case occurs for $[Ag_9Cu_6(C{\equiv}C\text{-}CH_3)_{11}]^+$ and $[Au_2Ag_8Cu_5(C{\equiv}C\text{-}CH_3)_{11}]^+$.

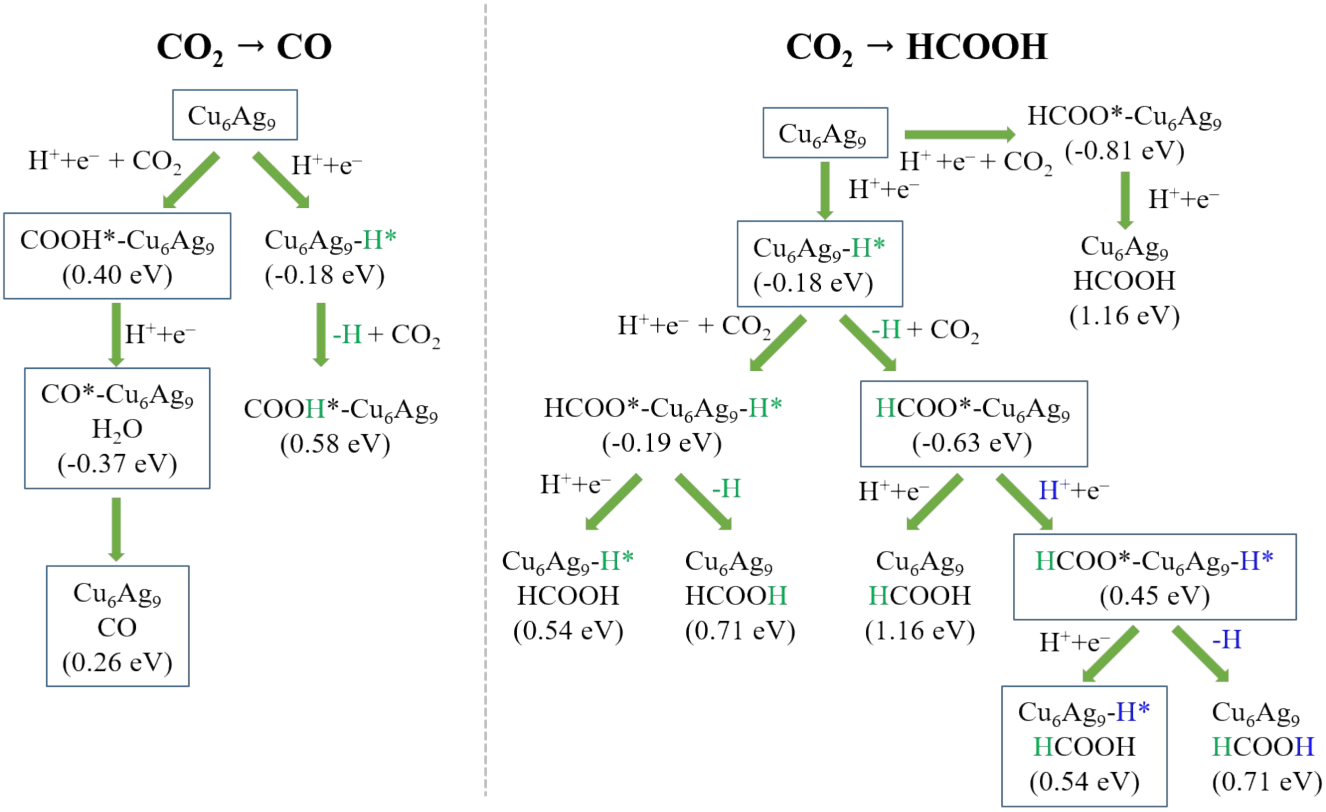

Figure S22. Reaction scheme for CO_2 electroreduction on $[Ag_9Cu_6(C{\equiv}C\text{-}CH_3)_{11}]^+$ to form CO and formate. The most favorable reaction pathway is highlighted with the blue box; the first H* is marked in green and the second H* is marked in blue.

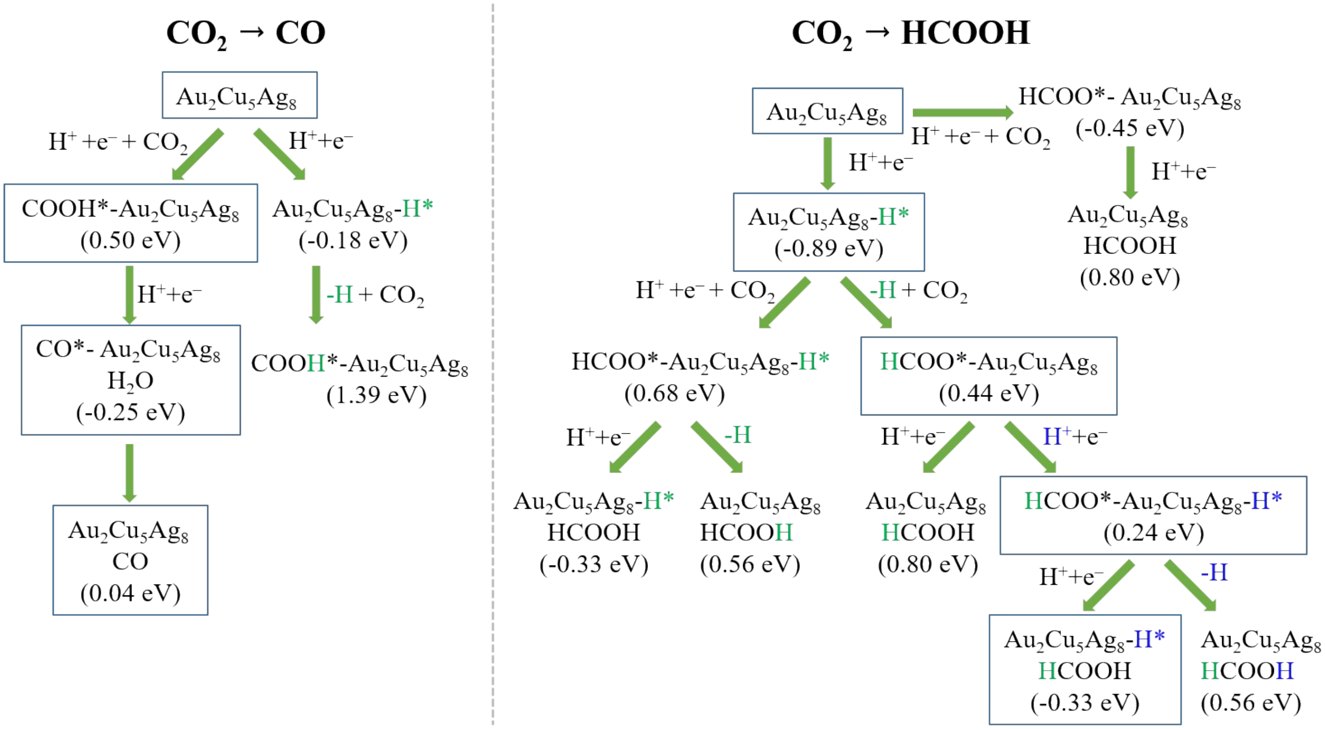

Figure S23. Reaction scheme for CO_2 electroreduction on $[Au_2Ag_8Cu_5(C{\equiv}C\text{-}CH_3)_{11}]^+$ to form CO and formate. The most favorable reaction pathway is highlighted with the blue box; the first H* is marked in green and the second H* is marked in blue.

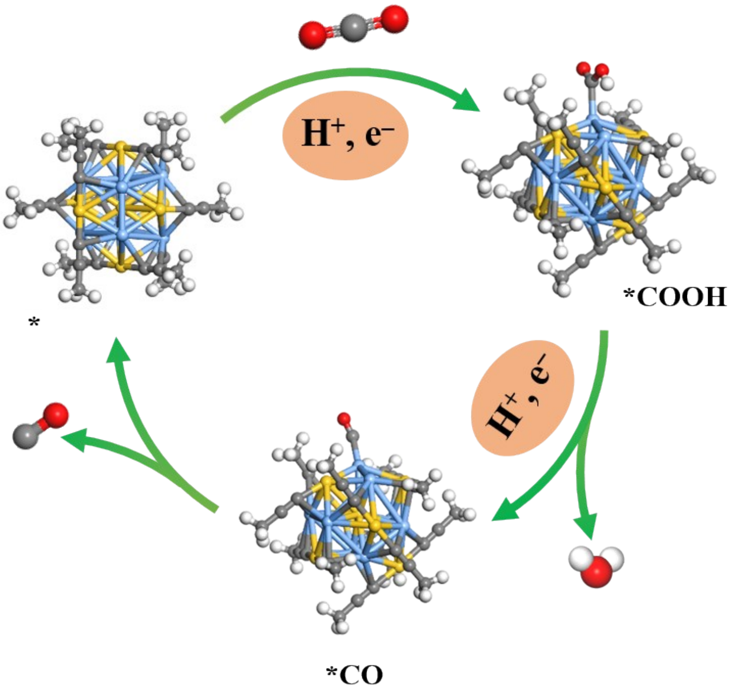

Figure S24. The overall mechanism of CO formation from CO_2 reduction on $[Au_7Ag_8(C{\equiv}C\text{-}CH_3)_{11}]^+$ via the proton mechanism. Color legend: Au, gold; Ag, blue; Cu, brick-red; C, gray; O, red; H, white.

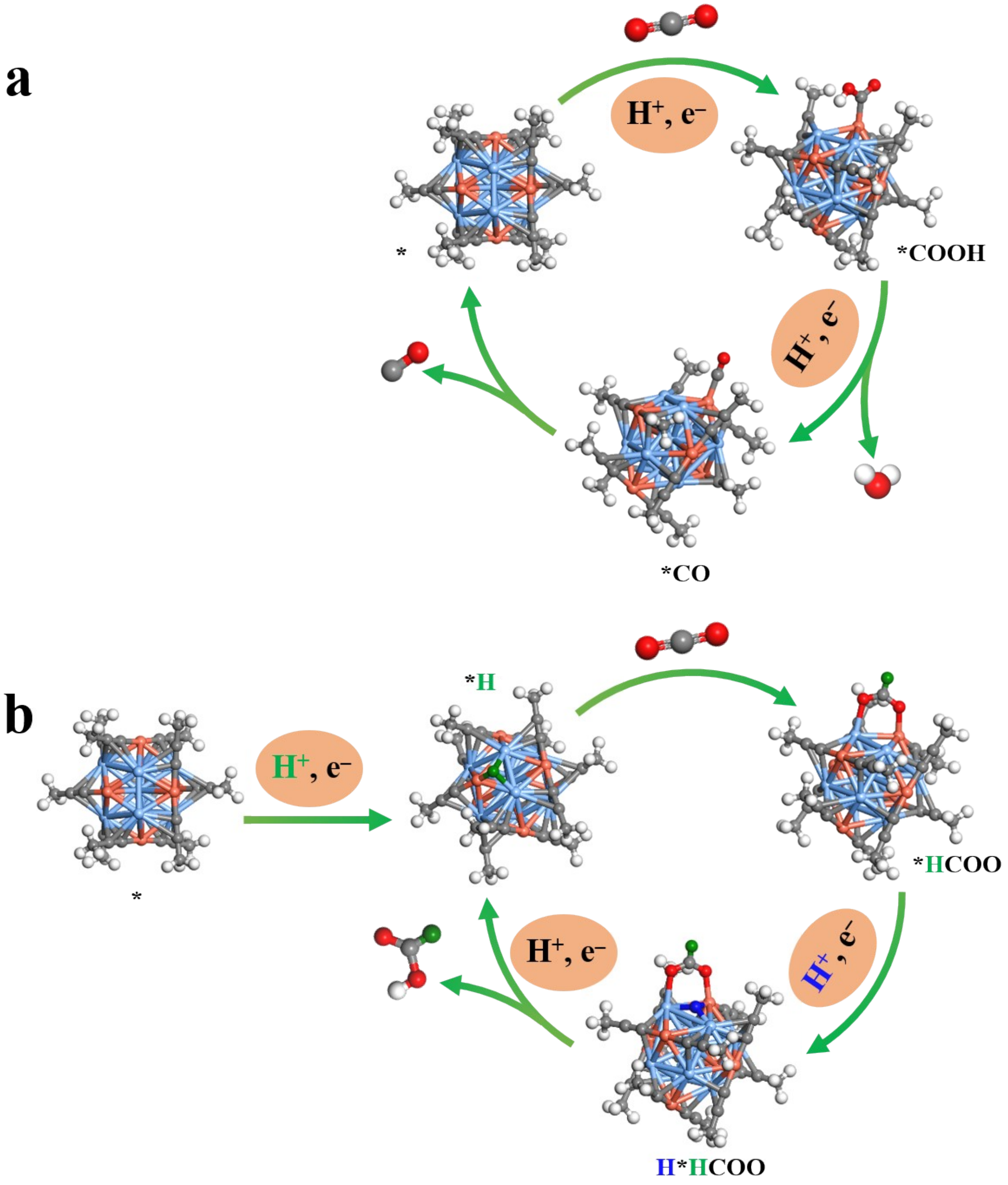

Figure S25. The overall mechanism of (a) CO formation via the proton mechanism and (b) formate formation via the hydride-proton mechanism from CO_2 reduction on $[Ag_9Cu_6(C{\equiv}C\text{-}CH_3)_{11}]^+$. Color legend: Au, gold; Ag, blue; Cu, brick-red; C, gray; O, red; H, white (mark the first H* in green and the second H* in blue).

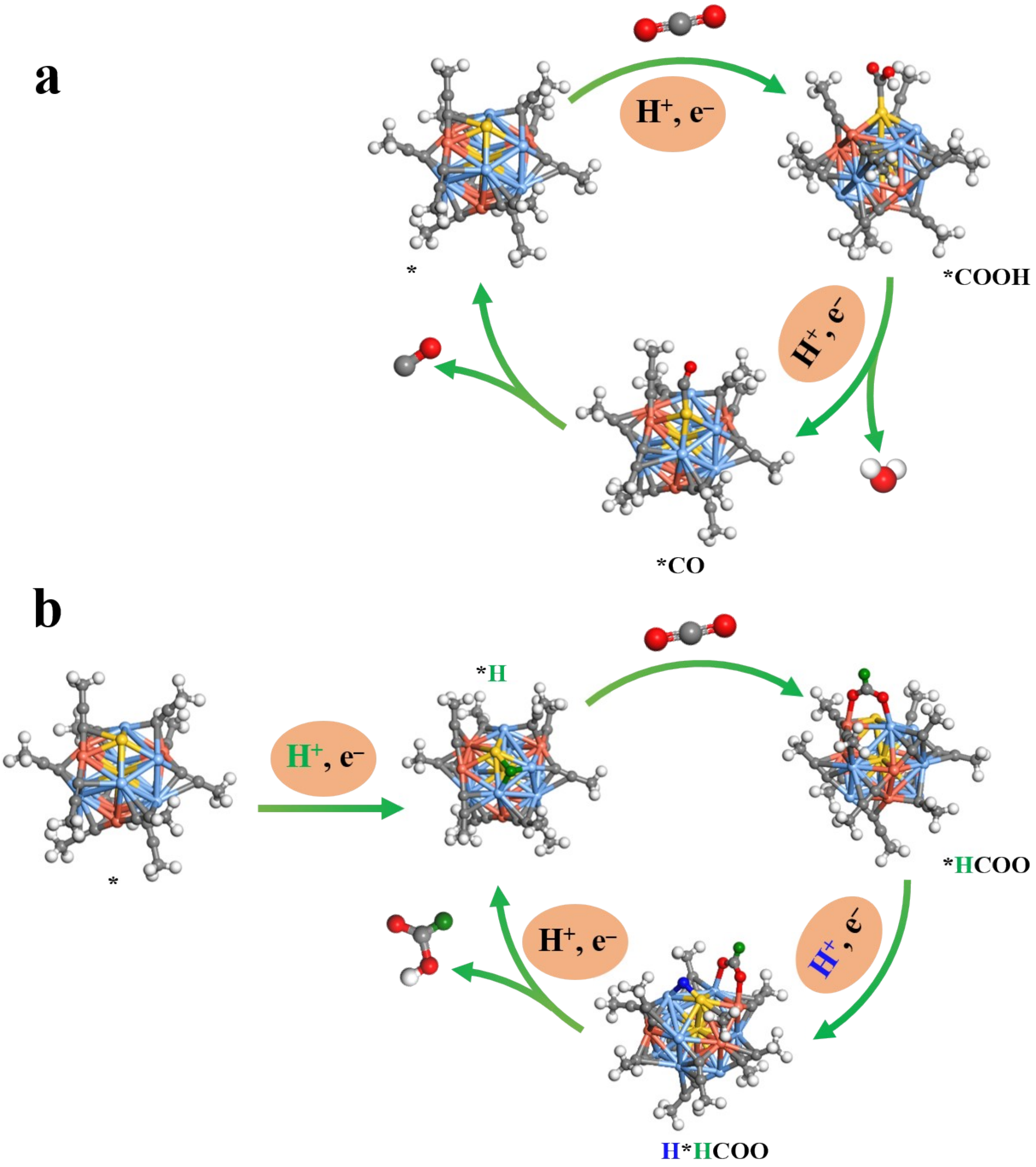

Figure S26. The overall mechanism of (a) CO formation via the proton mechanism and (b) formate formation via the hydride-proton mechanism from CO_2 reduction on $[Au_2Ag_8Cu_5(C\equiv C\text{-}CH_3)_{11}]^+$. Color legend: Au, gold; Ag, blue; Cu, brick-red; C, gray; O, red; H, white (mark the first H* in green and the second H* in blue).

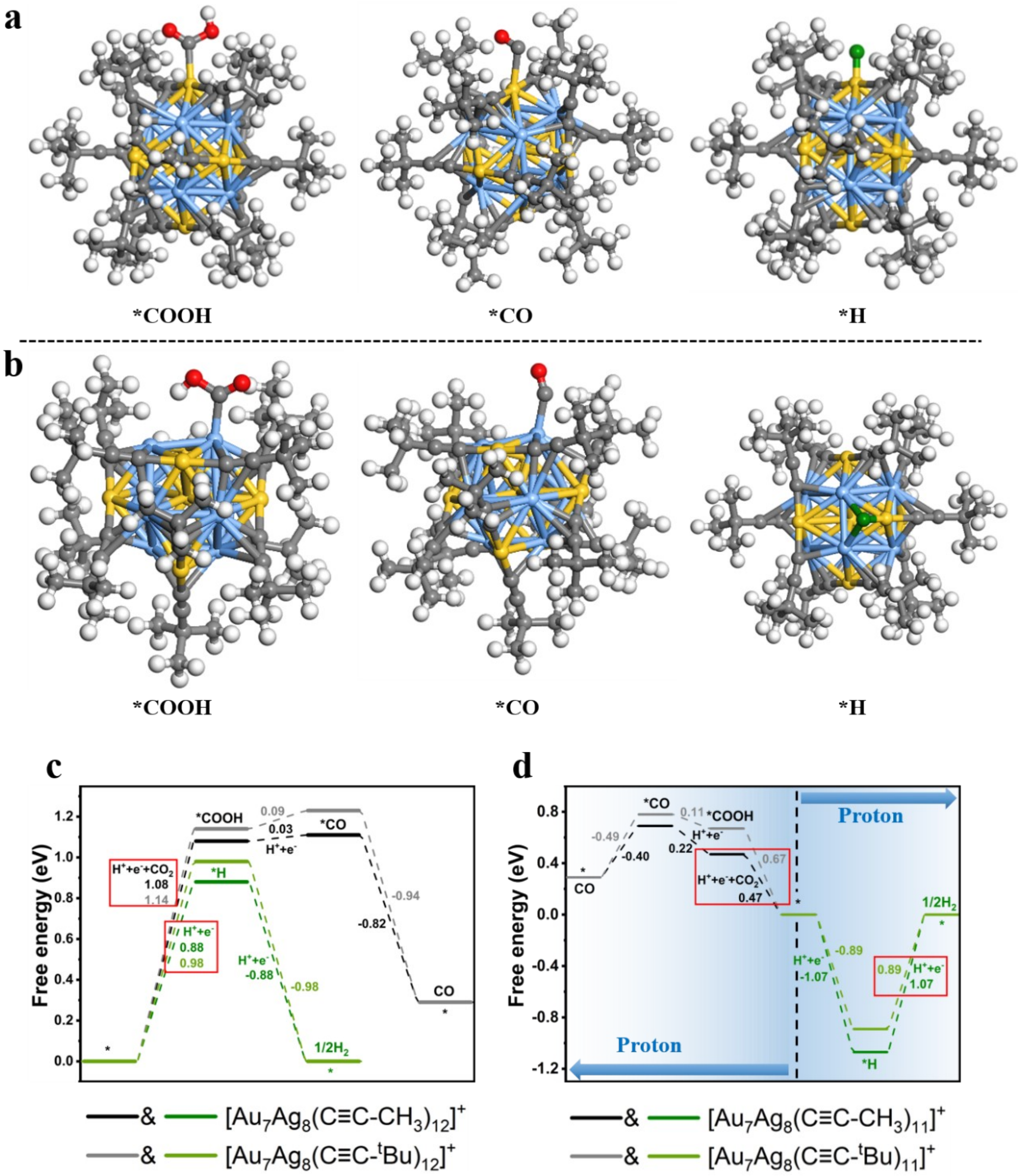

Figure S27. Schematic presentation of adsorption structures of *COOH, *CO and *H intermediates on (a) $[Au_7Ag_8(C{\equiv}C\text{-}^tBu)_{12}]^+$ and (b) $[Au_7Ag_8(C{\equiv}C\text{-}^tBu)_{11}]^+$ NCs, respectively. (c-d) Comparison of CO_2RR vs. HER on Au_7Ag_8 with $\text{-}C{\equiv}C\text{-}^tBu$ and $\text{-}C{\equiv}C\text{-}CH_3$ ligand protection. Color legend: Au, gold; Ag, blue; C, gray; O, red; *H, green; other H, white.

Supporting Tables

Table S1. The XPS data of $Au_2Ag_8Cu_5$ NCs.

Sample	**Au $4f_{5/2}$ (eV)**	**Au $4f_{7/2}$ (eV)**	**Ag $3d_{3/2}$ (eV)**	**Ag $3d_{5/2}$ (eV)**	**Cu $2p_{1/2}$ (eV)**	**Cu $2p_{3/2}$ (eV)**	**Au/Ag/Cu ratio**	
							Exp.	**Cal.**
$Au_2Ag_8Cu_5$	88.04	84.43	374.87	368.87	953.31	933.40	1.85/8.12/5.30	2/8/5

Table S2. Molar absorption coefficients (ε) of $Au_2Ag_8Cu_5$ NC.

Sample	**Molecular weight (M, g·mol^{-1})**	**Wavelength (λ_{max}, nm)**	**Absorbance (A)**	**Concentration (c, M)**	**Absorption coefficient (ε, M^{-1}·cm^{-1})**
$Au_2Ag_8Cu_5$	2784.02	484	0.84	4.49×10^{-5}	1.88×10^{4}

Table S3. Summary of the calculated yields of $Au_2Ag_8Cu_5$ NC.

Amount of reactants (mol)	**Concentration of sample (M)**	**Amount of $Au_2Ag_8Cu_5$ in reaction (mol)**	**Yield**
1.95×10^{-6} (Ag_9Cu_6 NC)	4.25×10^{-5}	1.70×10^{-6}	66.85% (based on Cu)

The calculation process of the yields of $Au_2Ag_8Cu_5$:

Sample:

$$c_{Au2Ag8Cu5} = \frac{0.80}{1.88 \times 10^{4}(M^{-1}cm^{-1}) \times 1(cm)} = 4.25 \times 10^{-5}\,(M)$$

Reaction solution:

$$n_{Au2Ag8Cu5} = \frac{4.25 \times 10^{-5}(M) \times 4(mL) \times 10(mL)}{1(mL)} = 1.70 \times 10^{-6}(mol)$$

The yield of product based on Cu:

$$Y_{Au2Ag8Cu5} = \frac{1.70 \times 10^{-6}(mol) \times 11.41\%}{1.95 \times 10^{-6}(mol) \times 14.88\%} \times 100\% = 66.85\%$$

Table S4. The mulliken charges analysis of Ag_9Cu_6.

Atom	Mulliken charges	Atom	Mulliken charges	Atom	Mulliken charges
Ag(1)	0.149	C(30)	0.122	H(59)	0.124
Ag(2)	0.161	C(31)	-0.335	H(60)	0.123
Ag(3)	0.171	C(32)	-0.326	H(61)	0.124
Ag(4)	0.172	C(33)	0.114	H(62)	0.125
Ag(5)	0.149	C(34)	-0.097	H(63)	0.142
Ag(6)	0.159	C(35)	-0.111	H(64)	0.125
Ag(7)	0.158	C(36)	0.111	H(65)	0.14
Ag(8)	0.163	C(37)	-0.33	H(66)	0.125
Ag(9)	**-0.004**	C(38)	-0.324	H(67)	0.124
Cu(10)	-0.352	C(39)	0.114	H(68)	0.144
Cu(11)	-0.341	C(40)	-0.113	H(69)	0.124
Cu(12)	-0.35	C(41)	-0.105	H(70)	0.14
Cu(13)	-0.342	C(42)	0.119	H(71)	0.126
Cu(14)	-0.347	C(43)	-0.328	H(72)	0.129
Cu(15)	-0.334	C(44)	-0.336	H(73)	0.142
C (16)	-0.109	C(45)	0.121	H(74)	0.125
C (17)	-0.106	C(46)	-0.111	H(75)	0.126
C (18)	0.112	C(47)	-0.097	H(76)	0.125
C (19)	-0.329	C(48)	0.117	H(77)	0.123
C (20)	-0.337	C(49)	-0.326	H(78)	0.143
C (21)	0.121	C(50)	-0.326	H(79)	0.127
C (22)	-0.099	C(51)	0.113	H(80)	0.137
C (23)	-0.106	H(52)	0.125	H(81)	0.135
C (24)	0.112	H(53)	0.123	H(82)	0.139
C (25)	-0.323	H(54)	0.143	H(83)	0.126
C (26)	-0.326	H(55)	0.136	H(84)	0.134
C (27)	0.116	H(56)	0.127	H(85)	0.124
C (28)	-0.108	H(57)	0.137	H(86)	0.143
C (29)	-0.106	H(58)	0.141	H(87)	0.124

Table S5. The crystal structure parameters for $[Au_2Ag_8Cu_5(C{\equiv}CBu^t)_{12}]SbF_6$.

Identification code	$[Au_2Ag_8Cu_5(C{\equiv}CBu^t)_{12}]$ SbF_6
Empirical formula	$C_{72}H_{108}Au_2Ag_8Cu_5F_6Sb_1$
Formula weight	2784.22
Temperature/K	149.99(10)
Crystal system	Trigonal
Space group	*R*
a/Å	16.1854(6)
b/Å	16.1854(6)
c/Å	28.7700(18)
α/°	90
β/°	90
γ/°	120
Volume/Å^3	6527.1(6)
Z, Calculated density/ Mg/m^3	3.00006, 2.125
Absorption coefficient/ mm^{-1}	6.656
F(000)	3972
Crystal size/mm^3	0.02 × 0.04 × 0.06
Radiation	CuK_α ($\lambda = 1.54184$)
2θ range for data collection/°	3.183 to 28.988
Index ranges	$-19 \leq h \leq -22$, $-21 \leq k \leq 21$, $-39 \leq l \leq 36$
Reflections collected	18840
Independent reflections	3641 [R(int) = 0.0687]
Data/restraints/parameters	3641/ 55/ 149
Goodness-of-fit on F^2	1.051
Final R indexes [I≥2σ (I)]	$R_1 = 0.0737$, $wR_2 = 0.1776$
Final R indexes [all data]	$R_1 = 0.1468$, $wR_2 = 0.2231$
Largest diff. peak/hole / e Å^{-3}	3.145/ -2.266

Table S6. A summary of σ(Cu/Ag-C) and π (Au/Ag/Cu-C) bond lengths in motif 1, 2, 3, 4 and 5 on the surface of $Au_2Ag_8Cu_5$ NC.

Species	The range length of σ (M-C) bond (Å)	The average lengths of σ (M-C) bond (Å)	The range length of π (M-C) bond (Å)	The average lengths of π (M-C) bond (Å)
Motif 1	Ag1/Ag2-C 1.890 ~ 1.897	Ag1-C 1.894	Ag/ Cu-C 2.387 ~ 2.397	Ag/ Cu-C 2.392
Motif 2	Ag3-C 1.891 ~ 1.896	Ag3-C 1.893	Au/ Ag/ Cu-C 2.386 ~ 2.560	Au/ Ag/ Cu-C 2.395
Motif 3	Ag4-C 1.890 ~ 1.897	Ag1-C 1.894	Au/ Ag/ Cu-C 2.387 ~ 2.559	Au/ Ag/ Cu-C 2.398
Motif 4	Cu1-C 1.858 ~ 1.888	Cu1-C 1.873	Au/ Ag/ Cu-C 2.355 ~ 2.561	Au/ Ag/ Cu-C 2.394
Motif 5	Cu2-C 1.855 ~ 1.885	Cu2-C 1.870	Ag/ Cu-C 2.385 ~ 2.393	Ag/ Cu-C 2.389

Table S7. A summary of σ and π bond lengths in motifs on the surface of Au_7Ag_8, Ag_9Cu_6 and $Au_2Ag_8Cu_5$ NCs.

Species	The range length of σ (M-C) bond (Å)	The average lengths of σ (M-C) bond (Å)	The range length of π (M-C) bond (Å)	The average lengths of π (M-C) bond (Å)
Motif of Au_7Ag_8	Au-C 1.979 ~ 1.984	Au-C 1.982	Ag-C 2.490 ~ 2.564	Ag-C 2.513
Motif of Ag_9Cu_6	Cu-C 1.855 ~ 1.885	Cu-C 1.870	Ag-C 2.355 ~ 2.400	Ag-C 2.381
Motif of $Au_2Ag_8Cu_5$	Cu/ Ag-C 1.855 ~ 1.897	Cu/ Ag-C 1.886	Au/ Ag/ Au-C 2.355 ~ 2.563	Au/ Ag/ Au-C 2.394

Table S8. Lengths of bonds spread on different layer of $M_{core}@M_{cube}@M_{octahedron}$ structure in $Au_2Ag_8Cu_5$, Ag_9Cu_6, and Au_7Ag_8 NCs.

NCs	M_{core}-M_{cube} (Å)	M_{core}-$M_{octahedron}$ (Å)	M_{cube}-M_{cube} (Å)	M_{cube}-$M_{octahedron}$ (Å)	$M_{octahedron}$-C_{ligand} (Å)	M_{cube}-C_{ligand} (Å)
$Au_2Ag_8Cu_5$	2.957	3.297	3.414	2.890	1.886	2.394
Ag_9Cu_6	2.886	3.171	3.333	2.796	1.870	2.381
Au_7Ag_8	2.843	3.405	3.283	2.913	1.982	2.521

Table S9. Recovery of the Ag_9Cu_6 catalyst after CO_2RR test at applied potentials (the absorbance value of the original Ag_9Cu_6 catalyst was 0.385).

Potential (V vs. RHE)	**Absorbance after reaction (A)**	**Recycling amount of Ag_9Cu_6 (n, mol)**	**Recovery (%)**
-0.39	0.372	4.77×10^{-5}	96.6%
-0.49	0.361	4.63×10^{-5}	93.7%
-0.59	0.316	4.05×10^{-5}	82.0%
-0.79	0.142	1.82×10^{-5}	36.8%
-0.99	0.122	1.56×10^{-5}	31.6%
-1.19	0.117	1.50×10^{-5}	30.4%

Table S10. Recovery of the $Au_2Ag_8Cu_5$ catalyst after CO_2RR test at applied potentials (the absorbance value of the original $Au_2Ag_8Cu_5$ catalyst was 0.862).

Potential (V vs. RHE)	**Absorbance after reaction (A)**	**Recycling amount of Ag_9Cu_6 NCs (n, mol)**	**Recovery (%)**
-0.39	0.740	3.94×10^{-5}	89.7%
-0.49	0.738	3.93×10^{-5}	89.5%
-0.59	0.573	3.05×10^{-5}	69.5%
-0.79	0.283	1.51×10^{-5}	34.4%
-0.99	0.210	1.12×10^{-5}	25.5%
-1.19	0.173	0.92×10^{-5}	21.0%

Table S11. The formate-selectivity comparison of recently reported atomically precise metal nanoclusters in CO_2RR.

Catalyst	**Cell type**	**Electrolyte**	**Potential (V_{RHE})**	**$FE_{formate}$ (%)**	**Ref.**
$[Ag_9Cu_6(C{\equiv}C\text{-}{}^tBu)_{12}]^+$	Flow-cell	1.0 M KOH	-1.19	47.0	**This work**
$[Au_2Ag_8Cu_5(C{\equiv}C\text{-}{}^tBu)_{12}]^+$			-0.99	28.3	
$Au_{25}(PET)_{18}$	H-cell	1.0 M $KHCO_3$	-0.30	~20.0	11
$Au_{24}Cd_1(PET)_{18}$ *(PET= 2-Phenylethanethiol)*			-0.30	14.0	
$Au_{19}Cd_3(S\text{-}tol)_{18}$ *(S-tol = p-toluenethiol)*			-0.50	~10.0	
$Au_{38}Cd_4(d\text{-}MBT)_{30}$ *(d-MBT= 3, 5-Dimethylthiophenol)*			-0.30	~8.0	
$Cu_{32}H_{20}(S_2P(O^iPr_2)_2)_{12}$	H-cell	0.1 M $KHCO_3$ and 0.4 M KCl	-0.53	89.0	12

Table S12. The CO-selectivity comparison of recently reported atomically precise metal nanoclusters in CO_2RR.

Catalyst	Cell type	Electrolyte	Potential (V_{RHE})	FE_{CO} (%)	J_{CO} (mA·m^{-2})	Ref.
$[Au_7Ag_8(C{\equiv}C\text{-}^tBu)_{12}]^+$	Flow-cell	1 M KOH	-0.49	98.1	-156.5	**This work**
$[Ag_9Cu_6(C{\equiv}C\text{-}^tBu)_{12}]^+$			-0.49	94.2	-41.8	
$[Au_2Ag_8Cu_5(C{\equiv}C\text{-}^tBu)_{12}]^+$			-0.49	95.0	-26.4	
$[Ag_{15}(C{\equiv}C\text{-}^tBu)_{12}]^+$	H-cell	0.5 M $KHCO_3$	-0.60	95.0	13.0	13
$[Au_{28}(Ph\text{-}form)_{12}]^{2+}$ *(Ph-form= N, N'-Diphenylformamidine)*	H-cell	0.5 M $KHCO_3$	-0.57	96.5	N/A	14
$[Au_{55}(p\text{-}MBT)_{24}(Ph_3P)_6]^{3+}$ *(p-MBT= 4-methylbenzenethiolate)*	H-cell	0.1 M $KHCO_3$	-0.60	94.1	N/A	15
$Au_{25}(PET)_{18}$ *(PET= 2Phenylethanethiol)*	H-cell	1.0 M $KHCO_3$	-0.40	70.0	-7.0	11
$Au_{24}Cd_1(PET)_{18}$			-0.50	90.0	-18.1	
$Au_{19}Cd_3(S\text{-}tol)_{18}$ *(S-tol= p-Toluenethiol)*			-0.50	~63.0	-2.3	
$Au_{38}Cd_4(d\text{-}MBT)_{30}$ *(d-MBT= 3,5-Dimethylthiophenol)*			-0.50	~58.0	-10.8	
$Au_{25}(PET)_{18}$	H-cell	0.5 M $KHCO_3$	-0.80	~100.0	~-33.0	16
$Au_{25}(Nap)_{18}$ *(Nap= 1-Naphthalenethiolate)*			-0.80	~100.0	~-28.0	
$Au_{25}(SePh)_{18}$			-0.50	~90.0	~-22.0	
$Au_{25}(SC_6H_{13})_{18}$	Flow-cell	3.0 M KOH	-0.30	~90.0	59.0	17
$Au_{38}(SC_6H_{13})_{24}$			-0.30	~90.0	~100.0	
$Au_{144}(SC_6H_{13})_{60}$			-0.30	~90.0	230.0	
$Au_{23}(SR)_{16}$ *(SR= cyclohexanethiolate)*	H-cell	0.5 M $KHCO_3$	-0.60	65.0	~-25.0	18
$Au_{19}Cd_2(SR)_{16}$			-0.90	95.0	~-45.0	
$Au_{47}Cd_2(TBBT)_{31}$ *(TBBTH= 4-tert-butylbenzenelthiol)*	H-cell	0.5 M $KHCO_3$	-0.57	96.0	-3.2	19
$Au_{44}(TBBT)_{28}$			-0.57	83.0	-1.6	
$[AuAg_{26}(S\text{-}Adm)_{18}S]^-$ *(HS-Adm= 1-adamantanethiolate)*	H-cell	Cathode: EMIM-BF_4/H_2 (V/V=7/1); Anode: 0.5 M H_2SO_4	-0.97	98.4	~13.0	20
$[Ag_{25}(DMT)_{18}]^-$ *(DMT= 2,4-dimethylbenzenethiol)*			-0.97	~54.6	~4.0	
$Au_{21}(S\text{-}Adm)_{16}$			-0.97	~4.1	~2.0	
$Pd_1Au_{24}(PET)_{18}$	H-cell	0.1 M $KHCO_3$	-1.20	~100.0	20.3	21
$Au_{25}(PET)_{18}$			-0.90	~100.0	~19.0	
Sphere-like Au_{25}	H-cell	0.1 M $KHCO_3$	-0.57	73.7	~100.0	22
Rod-like Au_{25}			-0.57	28.0	~43.0	
$Cu_{32}H_{20}L_{12}$ $(L = S_2P(O^iPr)_2)$	H-cell	0.1 M $KHCO_3$ and 0.4 M KCl	-0.63	3.0	N/A	12

$Au_{24}Ag_{20}(C_{12}H_{13})_{24}Cl_2$	H-cell	0.5 M $KHCO_3$	-0.50	90.0	N/A	23
$Au_{43}Ag_{38}(C_{12}H_{13})_{36}Cl_{12}$				~75.0	N/A	
$Au_{24}Ag_{20}(C_9H_7)_{24}Cl_2$				~90.0	N/A	
$Au_{43}Ag_{38}(C_9H_7)_{36}Cl_9$				~70.0	N/A	
$[Au_{22}H_3(dppe)_3(PPh_3)_8]^{3+}$ *(dppe= 1,2-bis(diphenylphosphino)ethane)*	H-cell	0.5 M $KHCO_3$	-0.60	92.7	N/A	24
$[Au_{11}(dppe)_5]^{3+}$			-0.60	70.6	N/A	

Table S13. Bader charges on the metal active atom bonded to *H.

	Au_7Ag_8	**Ag_9Cu_6**	**$Au_2Ag_8Cu_5$**
Bader charge (metal site)/|e|	Au (0.18)	Cu (0.46)	Au (-0.15)
Bader charge (H*)/|e|	-0.14	-0.29	-0.08